Editor invited article

Effect of damage evolution on the auxetic behavior of 2D and 3D re-entrant type geometries

Chetna Srivastava [a], Vinyas Mahesh [e], P.J. Guruprasad [b], Nik Petrinic [c], Fabrizio Scarpa [d], Dineshkumar Harursampath [a], Sathiskumar A. Ponnusami [e,*]

[a] *Department of Aerospace Engineering, Indian Institute of Science, Bengaluru, 560012, India*
[b] *Department of Aerospace Engineering, Indian Institute of Technology Bombay, Mumbai, 400076, India*
[c] *Department of Engineering Science, University of Oxford, Parks Road, Oxford, OX1 3PJ, United Kingdom*
[d] *Bristol Composites Institute, University of Bristol, BS8 1TR, Bristol, United Kingdom*
[e] *Department of Engineering, City, University of London, Northampton Square, EC1V 0HB, London, United Kingdom*

A R T I C L E   I N F O

A B S T R A C T

In this work, a mathematical formulation based on variational asymptotic method (VAM) has been proposed to determine the effect of damage on the auxetic properties of two-dimensional (2D) and three-dimensional (3D) re-entrant geometries. The influence of damage progression on the auxetic behavior was captured using a geometrically exact one-dimensional beam theory and an isotropic damage law, implemented in a nonlinear finite element framework. The effect of material degradation on the macroscale effective elastic properties such as the elastic modulus and Poisson's ratio for the two-dimensional and three-dimensional re-entrant auxetic geometries was quantified. The mechanical behavior as predicted by the in-house Python-based implementation of the proposed VAM-based formulation is verified with the results from the commercial finite element solver Abaqus, wherein the user material subroutine was used to capture damage evolution. The numerical examples presented in this paper reveal that the macroscale auxetic behavior of the geometries was affected significantly by damage progression. The results of this research will provide insights into the design and analysis of auxetic materials for applications that warrant consideration of damage evolution.

1. Introduction

Auxetic materials exhibit a negative value of Poisson's ratio (Kolken and Zadpoor, 2017), i.e., a longitudinal elongation for these materials is coupled with a lateral extension unlike conventional materials. These materials are fundamentally a tessellation of a unit cell or micro-structure. The peculiarity in their mechanical characteristics is attributed to the deformation mechanism of their micro-structure or unit cell. With recent advancements in additive manufacturing (Joseph et al., 2021), several different geometries of these unit cells have been the subject of various analytical, numerical, and experimental investigations (Smith et al., 2000; Tang et al., 2020; Gaspar et al., 2005; Remennikov et al., 2019; Koudelka et al., 2016; Elipe and Lantada, 2012; Rad et al., 2015; Dutta et al., 2021; Li et al., 2021; Jiang et al., 2019; Mukhopadhyay and Adhikari, 2016, 2017; Wei et al., 2020), while a number of studies have focused on design of novel geometries exhibiting a negative value of Poisson's ratio (Peng and Bargmann, 2021; Wei et al., 2020; Fu et al., 2018; Grima et al., 2005; Meena and Singamneni, 2021). Similar to naturally occurring materials, the characterization of auxetic materials involves determination of effective elastic properties, i.e., Young's modulus and Poisson's ratio (Mousanezhad et al., 2016; Scarpa et al., 2000; Gatt et al., 2013; Tabacu et al., 2020; Liu et al., 2020). Numerical homogenization has previously been used to determine effective elastic properties (Wang et al., 2018; Theocaris et al., 1997; Srivastava et al., 2023b), while a significant majority of previous works derive closed-form expressions for effective elastic properties in terms of geometric and material parameters by discretizing the auxetic microstructure into beams and imposing suitable boundary conditions to represent periodicity (Mousanezhad et al., 2016; Gatt et al., 2013).

Within the framework of small deformation theories such as the Euler–Bernoulli beam model, these expressions are independent of applied strain and stress fields, which is inconsistent with the experimentally observed strain-dependent behavior (Gao et al., 2018). Mechanical

---

Invited Editor: Ghatu Subhash.

* Corresponding author.

E-mail addresses: chetnas@alum.iisc.ac.in (C. Srivastava), Vinyas.Mahesh@city.ac.uk (V. Mahesh), nik.petrinic@eng.ox.ac.uk (N. Petrinic), f.scarpa@bristol.ac.uk (F. Scarpa), dineshkumar@iisc.ac.in (D. Harursampath), sathiskumar.ponnusami@city.ac.uk (S.A. Ponnusami).

behavior for these geometries under large far-field stresses can be predicted accurately using large deformation beam theories, wherein geometrically exact expressions for curvature are used in the moment equilibrium equations for the beam. Wan et al. (2004) used large deformation theory, i.e., the elastica theory, to determine the variation of Poisson's ratio with applied strain for the re-entrant type geometry shown in Fig. 2. Gao et al. (2018) used a similar methodology to determine strain-dependent mechanical behavior for the double-V geometry of the microstructure. In addition to one-dimensional non-linearity along the beam-reference line attributed to large displacements and rotation of the cross-section, as a consequence of large far-field stresses, the members constituting the micro-structure may also undergo significant damage as a consequence of material non-linearity. Within the framework of continuum damage mechanics pioneered by Kachanov (1999), the degradation of the material, i.e., the effect of micro-cracks, can be captured by defining an appropriate damage progression law to determine a damage variable. Computed as a function of material parameters and local stress and strain fields, the damage variable ranges between 0 to 1, representing an undamaged and completely damaged material state (Voyiadjis and Kattan, 2022).

While a majority of studies exist to quantify the elastic properties of a range of auxetic configurations, a very limited number of studies deal with analyzing the effect of damage evolution on the load-dependent behavior of auxetic materials. Previous works have focused on the deformation-dependent impact energy absorption characteristics of auxetics and sandwich panels with auxetic core wherein the improved performance of the auxetic materials relative to conventional materials has been highlighted (Zhang et al., 2020; Madke and Chowdhury, 2020; Wang, 2022; Najafi et al., 2021) and hence the design of auxetic microstructure geometries to enhance energy absorption characteristics has also been previously explored (Bohara et al., 2021). Some studies dealt with the geometric and material nonlinear mechanical behavior of auxetic materials (Seetoh et al., 2021; Du et al., 2022; Prajwal et al., 2022; Sabari et al., 2023). However, studies on explicit quantification of the influence of damage initiation and evolution on the auxeticity under large deformations are very limited. In this context, the present work utilizes a geometrically- and materially-nonlinear beam model, incorporating large deflections together with a material damage law, to quantify the effect of damage on the auxetic behavior.

The paper is organized as follows: Section 2 focuses on the analysis methodology comprising a geometrically nonlinear beam theory to model the damage evolution in 2D and 3D re-entrant auxetic materials using the variational asymptotic method (VAM). The results of the analysis are presented in detail in Section 3 together with a comparison to 3D finite element analysis results using Abaqus, followed by conclusions in Section 4.

2. Methodology

A geometrically nonlinear beam model coupled with a damage law is used to model the mechanical behavior of the ribs in the 2D and 3D auxetic structures considered in this study. In contrast to the conventional beam theories, the actual three-dimensional beam is reduced to an energetically equivalent one-dimensional problem without imposing ad-hoc kinematic assumptions,following the methodology proposed by Hodges (2006) and Yu et al. (2002). The VAM-based modeling framework shown in Fig. 1 is adopted in this work, followed by the integration of a damage law. In the context of the VAM formulation, the original three-dimensional problem is split into a two-dimensional cross-sectional analysis and a one-dimensional non-linear beam analysis, which accurately captures the in-plane as well as out-of-the-plane cross-sectional warping. As shown in Fig. 1, the cross-sectional stiffness matrix obtained from the two-dimensional analysis is a required input for one-dimensional non-linear beam analysis. As damage evolves along

the length of the inclined member, the stiffness coefficients corresponding to bending, twist and shear deformations would also exhibit degradation and thereby impact macroscale behavior for the geometry. The above damage-coupled geometrically nonlinear beam formulation is implemented in an in-house nonlinear finite element code developed in Python.

To demonstrate the effect of damage evolution on auxetic characteristics, the re-entrant type geometry (both in 2D and 3D) as shown in Fig. 2 is considered in the current work. For the re-entrant type geometry, it is the hinging of the inclined members, which affects the negative value of the Poisson's ratio at the macro-scale. The effective properties for the re-entrant type geometry of the microstructure are determined from the deformed configuration of the geometry under far-field stresses. The microstructure, as shown in Fig. 2 was discretized into beams with boundary conditions as outlined by Wan et al. (2004) and Levy et al. (2006), wherein, a large deflection model, i.e., the elastica theory, has been used to determine the effective value of Poisson's ratio under large far-field stresses, considering only the deformation of the inclined member AB as shown in Fig. 2 to be significant. Since the unit cell is part of a larger material medium, symmetry of deformation is imposed by suppressing rotations at joints A and B, thereby implying that the inclined beam AB can be broken into two half cantilever beams as indicated in Fig. 2.

With reference to Wan et al. (2004), the tip load on the cantilever beam, i.e. P_x, shown in Fig. 2, is estimated from the far-field stresses as per the following equation:

$$P_x = \sigma_x (H - L \sin \theta) t \tag{1}$$

where H and L are the lengths of the vertical and inclined members respectively, t is the width or thickness of the members and θ is the rib-inclination angle for the member as shown in Fig. 2. For larger deflections, the internal cell angle, i.e. θ for the geometry will change significantly, as the members deform, thereby indicating that Eq. (1), is valid over a limited range of applied stress, wherein the change in internal angles due to member deformation is not significant. However, in the present work Eq. (1) is used to determine the effective elastic modulus over the complete range of applied stress for the 2D re-entrant geometry, in order to estimate the change in effective stiffness for the material due to damage evolution. The tip deflection for the cantilever beams in horizontal and vertical directions, i.e. U_x and U_y, under the applied far-field stress σ_x would be determined for different values of rib-inclination angles θ, and the value of strains ϵ_x and ϵ_y is estimated as per the following equations from the deformed configuration of the geometry:

$$\epsilon_x = \frac{2U_x}{L \cos \theta} \quad \epsilon_y = \frac{2U_y}{H - L \sin \theta} \tag{2}$$

wherein $L \cos \theta$ and $(H - L \sin \theta)$ are the horizontal and vertical projections respectively of the undeformed inclined member AB. The macro-scale value of Poisson's ratio and effective elastic modulus in the x direction are estimated as per the following equations:

$$v_{xy} = -\frac{\epsilon_y}{\epsilon_x} = -\frac{U_y L \cos \theta}{U_x (H - L \sin \theta)} \tag{3}$$

$$E_x = \frac{\sigma_x}{\epsilon_x} = \frac{P_x L \cos \theta}{2(H - L \sin \theta) t U_x} \tag{4}$$

For comparison purposes, within the framework of linear beam theory, i.e. Euler–Bernoulli beam model for small deformation is used to obtain the value of v_{xy} and E_x, which are independent of applied stress or strain field. Accordingly, Eqs. (3) and (4), are reduced to the following form:

$$v_{xy} = \frac{(3 - k^2) \sin \theta}{[\alpha - \sin \theta][3 + k^2 \tan^2 \theta]} \tag{5}$$

$$E_x = \frac{12 E_s \delta_t}{[\alpha - \sin \theta] \cos \theta [k^2 \tan^2 \theta + 12]} \tag{6}$$
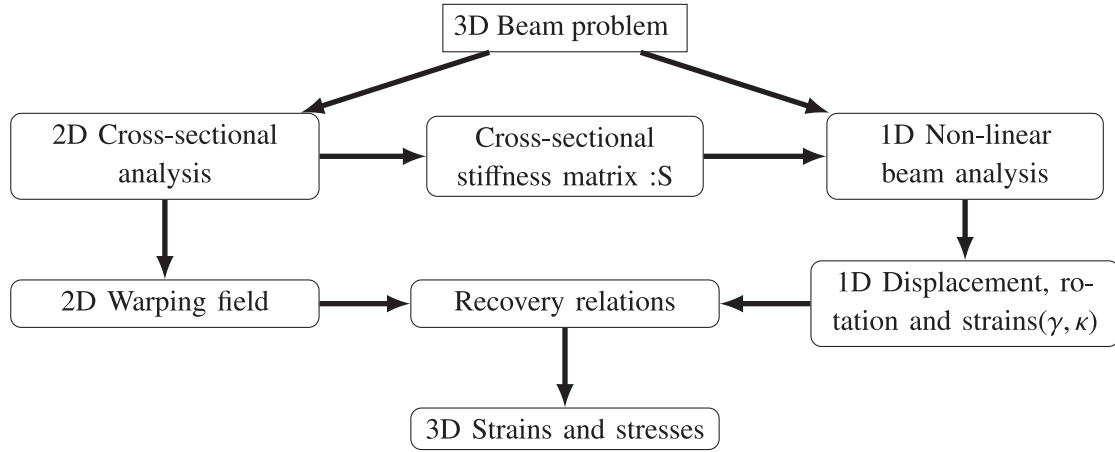
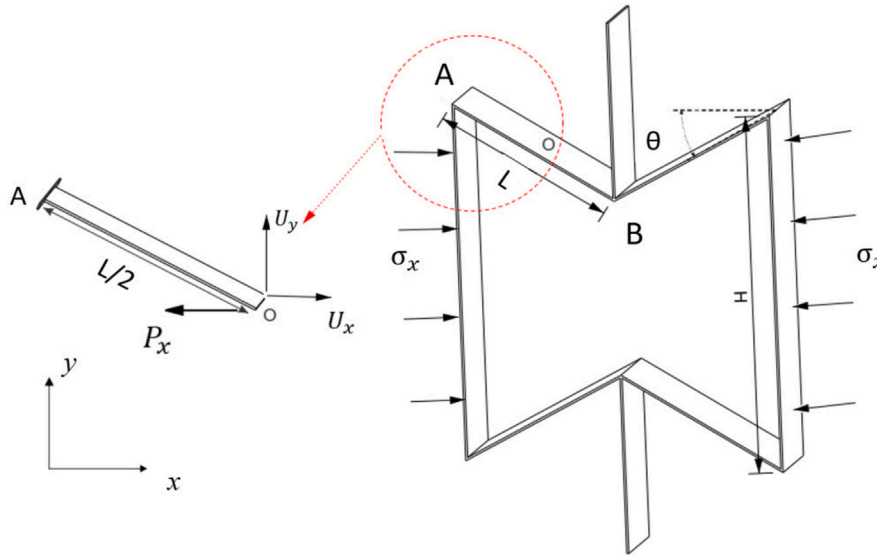Fig. 1. Methodology for beam analysis adopted in the present work as described by Hodges (2006).

Fig. 2. 2D re-entrant geometry with the inclination angle of the ribs θ, the length of inclined member L and height of vertical member H. Half-length cantilever beam model for the 2D re-entrant geometry (Wan et al., 2004): the inclined member AB is split into two half-length cantilever beams, i.e. AO and OB. The tip deflections in the horizontal and vertical directions for the cantilever beam are U_x and U_y, respectively. The tip load on the cantilever beam is determined from the applied far-field stress, i.e. σ_x Wan et al. (2004), Srivastava et al. (2023a).

where, k is the slenderness ratio of the half length cantilever beam AO, α is the ratio of the length of the vertical strut to the inclined strut, i.e. H/L, E_s is the value of Young's modulus for the material of the auxetic frame and δ_t is the ratio of the in-plane thickness of the member, i.e. t to the length of the member AB as shown in Fig. 2.

Similarly, for the case of 3D re-entrant geometry shown in Fig. 3, Yang et al. (2015) formulated analytical expressions for the Poisson's ratio and effective Young's modulus. Under the effect of applied far-field stresses in the vertical direction i.e. σ_z, the inclined members O_1E, O_2E, O_3E and O_4E deform symmetrically. Hence, from symmetry considerations, Yang et al. (2015) determined the value of Poisson's ratio from the deformed configuration of the inclined member O_1E and vertical member O_1O_4 as shown in Fig. 3, while restricting joint rotations at node O_1. Similar to the two-dimensional re-entrant geometry, the load on the half cantilever beam model for member O_1E is estimated from the far-field stress as per the following equations:

$$P_z = \frac{1}{2}\sigma_z L^2 \sin^2 \theta \tag{7}$$

The value of Poisson's ratio and effective modulus in the z direction, i.e. ν_{zx} and E_z for the three-dimensional geometry were determined

from the deformations of the inclined and vertical struts as per the following equation:

$$\nu_{zx} = -\frac{\epsilon_x}{\epsilon_z} = -\frac{2U_{x_1}(H - L\cos\theta)}{(2U_{z_1} + U_{z_2})L\sin\theta} \tag{8}$$

$$E_z = \frac{\sigma_z}{\epsilon_z} = \frac{2P_z(H - L\cos\theta)}{(2U_{z_1} + U_{z_2})L^2 \sin^2\theta} \tag{9}$$

where, H, L and θ are model parameters as shown in Fig. 3, U_{x_1} and U_{z_1} are the horizontal and vertical tip deflections for the half-length cantilever beam for member O_1E and U_{z_2} is the vertical deflection for the member O_1O_4. Again for comparison purposes, for small deformations, the Euler–Bernoulli beam model gives the following expression for the Poisson's ratio and effective modulus in the z-direction for the 3D geometry:

$$\nu_{zx} = -\frac{[k^2 - 12]\cos\theta[\alpha - \cos\theta]}{[k^2 \sin^2\theta + 12\cos^2\theta + 6\alpha]} \tag{10}$$

$$E_z = \frac{24E\delta_t^2[\alpha - \cos\theta]}{\sin^2\theta[k^2 \sin^2\theta + 12\cos^2\theta + 6\alpha]} \tag{11}$$

where, k, is the slenderness ratio for the inclined member O_1O_4. For slender struts, the Poisson's ratio for 2D re-entrant geometry was shown
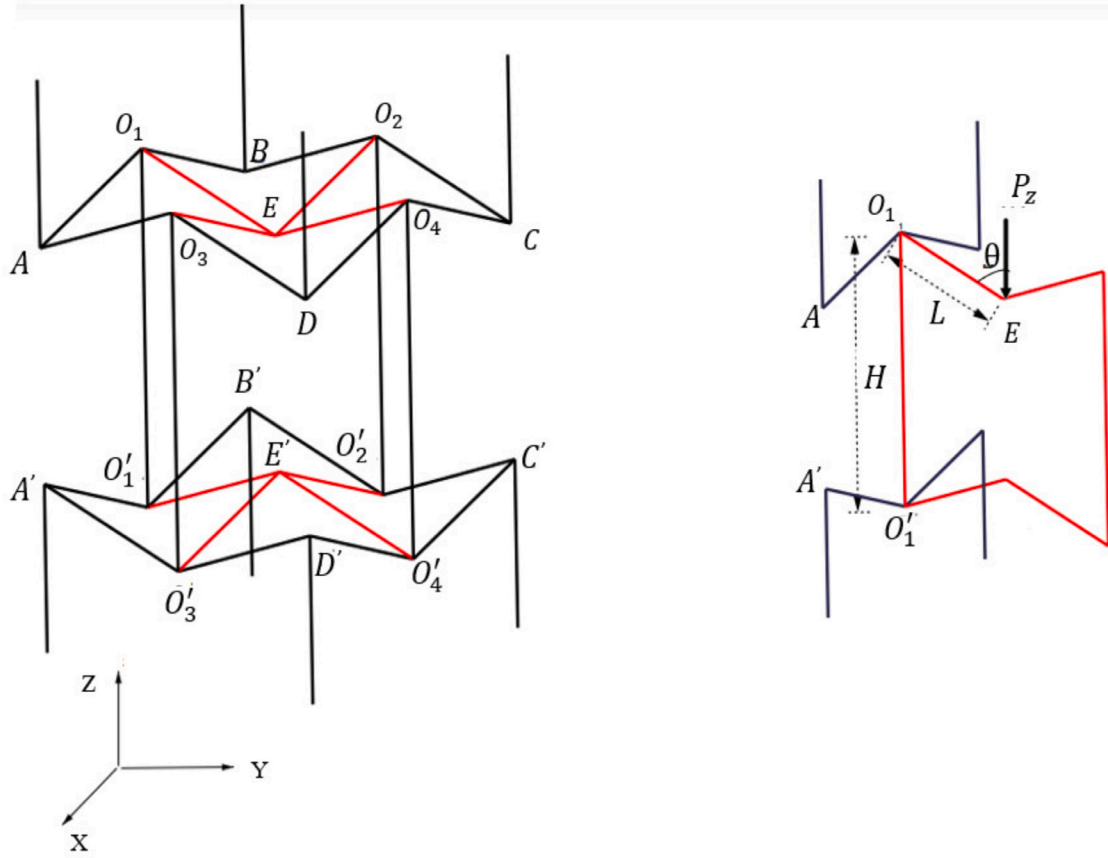
Fig. 3. 3D re-entrant geometry with the rib-inclination angle θ, length of inclined member L and height of vertical member H. The half-length cantilever beam model for the 3D re-entrant geometry: the inclined member is split into two half-length cantilever beams. The tip deflections in the horizontal and vertical directions for the cantilever beam are Δx_1 and Δz_1, respectively. The tip load on the cantilever beam is determined from the applied far-field stress σ_z (Yang et al., 2015; Srivastava et al., 2023a).

to vary significantly with applied strain (Wan et al., 2004). The deviation from the strain-independent value of Poisson's ratio determined from Eq. (5) was primarily attributed to large deformations, which have been previously accounted for using the elastica theory by Wan et al. (2004) and Levy et al. (2006), however, the results were obtained by considering physically unrealistic values of tip deflection angles as inputs. In contrast to the formulations presented in previous work for the geometry, in this work, the geometrically exact beam theory (GEBT) presented in Section 2.2 is used to determine deflections of the struts under large loads.

The material for the auxetic frame was assumed to be ABS plastic, which exhibits elastic plastic behavior (Hu et al., 2019), thereby implying that under the effect of far-field stresses, the material of the auxetic frame can potentially undergo significant damage. Hence, in addition to the impact of one-dimensional non-linearity due to the slenderness of the struts on the Poisson's ratio, the effect of material non-linearity due to excessive deformations and damage on the load-dependent mechanical behavior for the 2D and 3D re-entrant geometries is examined in the present work.

2.1. Cross sectional analysis

2.1.1. Beam kinematics

Consider the undeformed configuration of the beam as shown in Fig. 4, wherein b_i is an orthonormal triad of basis vectors, such that b_1 is along the beam reference line, which passes through the centroid of the cross section, while b_2 and b_3 are along two mutually perpendicular direction transverse to b_1. The position vector ($\hat{r}$) to a material point on the cross-section of the beam is thereby expressed in terms of the

measure numbers along b_1, b_2 and b_3 i.e.,

$$\hat{r}(x_1, x_2, x_3) = x_1 b_1 + x_2 b_2(x_1) + x_3 b_3(x_1) \tag{12}$$

where, x_1 is measured along the beam reference line and x_2, x_3 are measure numbers along b_2 and b_3, respectively to a material point on the undeformed cross section.

The position vector to the points of intersection of the cross-section with the beam reference line is denoted by r relative to the origin of the fixed frame A and the b_1 vector is tangential to the beam reference line, i.e.:

$$r' = b_1 \tag{13}$$

The derivatives of the orthonormal triad of b_i vectors with respect to x_1 are expressed as follows in terms of the initial curvature, i.e. k along the beam reference line:

$$b_i' = k \times b_i \tag{14}$$

Similarly, the position vector of a material point on the deformed cross section ($\hat{R}$) is given by the following expression (Hodges, 2006):

$$\hat{R} = r + u + x_2 B_2 + x_3 B_3 + w_i B_i \tag{15}$$

where $u(x_1)$ is the rigid body translation of the reference point i.e., point of intersection of the beam reference line and the cross-section, w_i is the warping field, B_1 is normal to the deformed beam cross-sectional plane, while B_2 and B_3, are mutually perpendicular, lying in the plane of the deformed cross-section also the vector B_1 is not tangential to the deformed reference line. The orthonormal triads b_i and B_i for the undeformed and deformed state respectively are related as per the following equation:

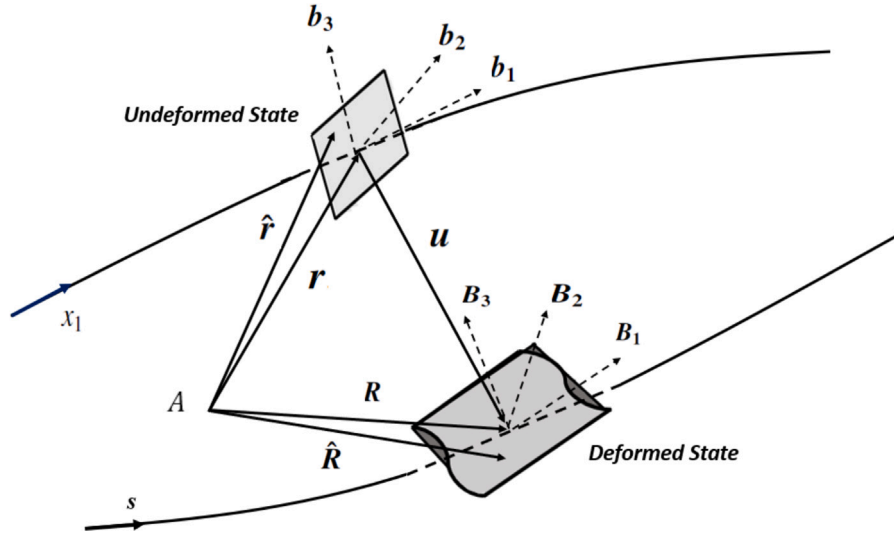$$b_i = \underline{C}^{bB} . B_i \tag{16}$$

Fig. 4. Undeformed and deformed configurations of the cross-section: position vector to a material point on the undeformed cross-section, i.e. $\hat{r}$ is expressed in terms of measure numbers along the orthonormal triad of b_i vectors, and the position vector to a material point on the deformed cross-section, i.e. $\hat{R}$ is expressed in terms of measure numbers along the orthonormal triad of B_i vectors.

where, $\underline{C}^{bB}$ is the rotation tensor. For the beam cross-sectional analysis, the three dimensional strain at a material point on the cross-section is expressed in terms of the one dimensional force and moment strains along the beam reference line, which are defined as follows:

$$\gamma = \underline{C}^{bB}.R' - r' \qquad (17)$$

$$\kappa = \underline{C}^{bB}.K - k \qquad (18)$$

where, K is the curvature of the deformed centerline of the beam, γ is the vector with force strains, κ is the vector with moment strains and $\underline{C}^{bB}$ is the rotation tensor. From Eqs. (17) and (16), the derivative of the position vector to the deformed centerline wrt. x_1 can be expressed as follows:

$$R' = (1 + \gamma_{11})B_1 + 2\gamma_{12}B_2 + 2\gamma_{13}B_3 \qquad (19)$$

where, γ_{11}, $2\gamma_{12}$ and $2\gamma_{13}$ are the measure numbers of the force strain vector in the b_i basis. Analogous to Eq. (14), the derivative of the B_i triad w.r.t x_1 can be written as follows in terms of the initial curvature k and moment strains κ:

$$B_i' = (\kappa + k) \times B_i \qquad (20)$$

In order to determine the three dimensional strains, the deformation gradient tensor ($\underline{X}$) is determined as per the following equation (Hodges, 2006):

$$\underline{X} = G_i g^i \qquad (21)$$

where, G_i are the covariant vectors for the deformed configuration and g^i are the contravariant vectors for the undeformed configuration. The position vectors as defined in Eqs. (12) and (15) are used to determine the covariant vectors in the undeformed (g_i) and deformed (G_i) state respectively in accordance with the following set of equations:

$$g_1 = \frac{\partial \hat{r}}{\partial x_1} \qquad g_2 = \frac{\partial \hat{r}}{\partial x_2} \qquad g_3 = \frac{\partial \hat{r}}{\partial x_3} \qquad (22)$$

$$G_1 = \frac{\partial \hat{R}}{\partial x_1} \qquad G_2 = \frac{\partial \hat{R}}{\partial x_2} \qquad G_3 = \frac{\partial \hat{R}}{\partial x_3} \qquad (23)$$

The contravariant vectors (g^i) are determined as follows from the covariant vectors (g_i) as per the following equation, where $\sqrt{g} = det(g_i.g_j)$:

$$g^i = \frac{\epsilon_{ijk}}{2\sqrt{g}} g_j \times g_k \qquad (24)$$

Further, in order to simplify the formulations for the three-dimensional strain components the orthonormal triad T_i is introduced, such that T_1 is tangential to the deformed center-line of the beam, and B_i and T_i vectors are related as follows:

$$\begin{bmatrix} B_1 \\ B_2 \\ B_3 \end{bmatrix} = \begin{bmatrix} 1 & -2\gamma_{12} & -2\gamma_{13} \\ 2\gamma_{12} & 1 & 0 \\ 2\gamma_{13} & 0 & 1 \end{bmatrix} \begin{bmatrix} T_1 \\ T_2 \\ T_3 \end{bmatrix} \qquad (25)$$

where, $2\gamma_{12}$ and $2\gamma_{13}$ are small angles due to shear deformation. Considering the T_i triad, the position vector to a material point in the deformed configuration can be re-expressed as follows:

$$\hat{R} = r + u + x_2 T_2 + x_3 T_3 + \bar{w}_i T_i \qquad (26)$$

In the T_i basis, since the shear strain is a part of the warping field, generalized one-dimensional strain measures of the classical theory are introduced as follows:

$$\bar{\epsilon} = \begin{bmatrix} \bar{\gamma}_{11} \\ \bar{\kappa}_1 \\ \bar{\kappa}_2 \\ \bar{\kappa}_3 \end{bmatrix} \qquad (27)$$

such that :

$$\bar{\gamma}_{11} = \gamma_{11}|_{(2\gamma_{1\alpha}=0)} \qquad (28)$$

$$\bar{\kappa}_i = \kappa_i|_{(2\gamma_{1\alpha}=0)} \qquad (29)$$

The deformation gradient tensor components, in the mixed basis are thereby expressed as follows:

$$X_{ij} = T_i.G_k g^k.b_j \qquad (30)$$

where, the covariant vectors for the deformed configuration can be determined by substituting Eq. (26) in Eq. (23). From the deformation gradient tensor, the three-dimensional strain components are computed as follows:

$$\Gamma_{ij} = \frac{X_{ij} + X_{ji}}{2} - \delta_{ij} \qquad (31)$$

The terms of the deformation gradient tensor and the three dimensional strain components have been summarized in the Appendix (ref. A.1). The three dimensional strains, after discarding the product of one-dimensional strain and warping can be written in the following matrix form:

$$\Gamma = \Gamma_a w + \Gamma_\epsilon \bar{\epsilon} + \Gamma_R w + \Gamma_l w' \qquad (32)$$

where $\Gamma = [\Gamma_{11} \quad 2\Gamma_{12} \quad 2\Gamma_{13} \quad \Gamma_{22} \quad 2\Gamma_{23} \quad \Gamma_{33}]^T$ and Γ_a, Γ_R, Γ_l and Γ_ϵ are coefficient matrices as summarized in Eq. (A.18). The warping field further satisfies the following constraint (Hodges, 2006):

$$\Gamma_a w = 0 \tag{33}$$

Using Eq. (32), the strain energy per unit length of the beam in terms of the three-dimensional strain can be determined using the following equation:

$$U = \frac{1}{2} \int_A \Gamma^T D \Gamma \sqrt{g} \, dx_2 dx_3 \tag{34}$$

where D is the material matrix that relates the stress and strain field at a material point. The terms of the material matrix D would undergo degradation as damage evolves. The degraded material parameters would be computed at each load step from the local strains as per the damage law for the material constituting the auxetic frame.

2.1.2. Zeroth order approximation

For a finite element implementation, the warping field is discretized as follows:

$$w = SV \tag{35}$$

where, V is the column matrix with nodal values of the three dimensional warping field and S is the shape function matrix. On substituting the discretized warping field in the expression for strain energy, i.e. Eq. (34), and retaining zeroth order terms, the following expression for the zeroth order strain energy functional is obtained:

$$2U_0 = V^T EV + 2V^T D_{a\epsilon} \bar{\epsilon} + \bar{\epsilon}^T D_{\epsilon\epsilon} \bar{\epsilon} \tag{36}$$

In Eq. (36), $D_{a\epsilon}$ and $D_{\epsilon\epsilon}$ are coefficient matrices for which the integral expressions have been summarized in Eq. (A.20). The zeroth order strain energy functional is minimized subject to the constraint in Eq. (33) using Lagrange's parameters to get the following Euler–Lagrange's equations:

$$EV = -D_{a\epsilon} \bar{\epsilon} \tag{37}$$

The detailed mathematical formulations for the Euler–Lagrange's equation have been summarized in the Appendix (ref. A.1.1). In order to solve the Euler–Lagrange's equation numerically, warping influence coefficients $\hat{V}_o$ are introduced, such that $V = \hat{V}_o \bar{\epsilon}$. and the 4 × 4 cross-sectional stiffness matrix ($\bar{S}$) is from the coefficient matrices:

$$\bar{S} = \hat{V}_o^T D_{a\epsilon} + D_{\epsilon\epsilon} \tag{38}$$

The zeroth order strain energy is expressed as follows in terms of the cross-sectional stiffness matrix:

$$U_o = \frac{1}{2} \begin{bmatrix} \bar{\gamma}_{11} & \bar{\kappa}_1 & \bar{\kappa}_2 & \bar{\kappa}_2 \end{bmatrix} \begin{bmatrix} \bar{S}_{11} & \bar{S}_{12} & \bar{S}_{13} & \bar{S}_{14} \\ \bar{S}_{12} & \bar{S}_{22} & \bar{S}_{23} & \bar{S}_{24} \\ \bar{S}_{13} & \bar{S}_{23} & \bar{S}_{33} & \bar{S}_{34} \\ \bar{S}_{14} & \bar{S}_{24} & \bar{S}_{34} & \bar{S}_{44} \end{bmatrix} \begin{bmatrix} \bar{\gamma}_{11} \\ \bar{\kappa}_1 \\ \bar{\kappa}_2 \\ \bar{\kappa}_3 \end{bmatrix} \tag{39}$$

2.1.3. First order approximation

For the first-order solution, the warping field determined from the zeroth-order solution is perturbed as shown below:

$$V = V_o + V_1 \tag{40}$$

Retaining the leading terms, removing constant terms from zeroth order approximation and integrating by parts, the strain energy with the perturbed warping field is obtained (ref, A.1);

$$2U_1 = V_1^T EV_1 + 2V_1^T D_R \bar{\epsilon} + 2V_1^T D_S \bar{\epsilon}' \tag{41}$$

The detailed mathematical formulations for the cross-sectional stiffness matrix as determined from first-order approximation for the warping field have been summarized in the Appendix (ref. A.1.2). The 6 × 6 cross-sectional stiffness matrix obtained from the procedure for beam cross-sectional analysis (Hodges, 2006), thereafter has the following

form such that, the one-dimensional strains along the beam reference line can be related to force resultants as per the following equations:

$$\begin{bmatrix} F_1 \\ F_2 \\ F_3 \\ M_1 \\ M_2 \\ M_3 \end{bmatrix} = \begin{bmatrix} S_{11} & S_{12} & S_{13} & S_{14} & S_{15} & S_{16} \\ S_{12} & S_{22} & S_{23} & S_{24} & S_{25} & S_{26} \\ S_{13} & S_{23} & S_{33} & S_{34} & S_{35} & S_{36} \\ S_{14} & S_{24} & S_{34} & S_{44} & S_{45} & S_{46} \\ S_{15} & S_{25} & S_{35} & S_{45} & S_{55} & S_{56} \\ S_{16} & S_{26} & S_{36} & S_{46} & S_{56} & S_{66} \end{bmatrix} \begin{bmatrix} \gamma_{11} \\ 2\gamma_{12} \\ 2\gamma_{13} \\ \kappa_1 \\ \kappa_2 \\ \kappa_2 \end{bmatrix} \tag{42}$$

2.2. Geometrically exact beam theory

The cross-sectional stiffness matrix obtained in Section 2.1 is used as an input for one-dimensional analysis along the beam reference line. The equations for one-dimensional beam analysis are derived from extended Hamilton's principle:

$$\int_{t_1}^{t_2} \int_0^L \left[\delta(T - U) + \delta\bar{W} \right] = \delta\bar{A} \tag{43}$$

where T is the kinetic energy per unit length, U is the strain energy per unit length, W is the virtual work done by the applied loads per unit length, and A, is the virtual action at the ends of the beam. The mathematical formulations for the Euler–Lagrange's equations and the finite element formulation for the one-dimensional analysis have been summarized in the Appendix (ref. B.1). From the 1D analysis, the one-dimensional strains (ref. Eqs. (17) and (18)) along the beam reference line, as determined from Eq. (42) at a given load increment are used to evaluate the local three-dimensional strains in accordance with the recovery relations (ref. Section 2.3), to determine the local degraded material property as per the damage law for the material constituting the auxetic frame at each material point. The degraded material properties are used to determine the cross-sectional stiffness matrix (ref. A.1) for the next load step as summarized in Fig. 5

2.3. Recovery relations and damage evolution

As summarized in Fig. 5, the results from the one-dimensional beam analysis are used to determine the three-dimensional local strain Γ in accordance with the following equation (Hodges, 2006) (ref. A.1):

$$\Gamma = \left[(\Gamma_a + \Gamma_R)(V_0 + V_{1R}) + \Gamma_\epsilon\right]\bar{\epsilon} + \left[(\Gamma_a + \Gamma_R)V_{1S} + \Gamma_\epsilon(V_0 + V_{1R})\right]\bar{\epsilon}' + \Gamma_l V_{1S}\bar{\epsilon}'' \tag{44}$$

The local degradation or damage of the auxetic material is captured by the damage parameter d, which is evaluated as a function of local strain in accordance with appropriate damage law (Xue and Kirane, 2021). The value of the damage parameter, i.e. d, is used to determine the local degraded value of Young's modulus :

$$E_d = (1 - d)E \tag{45}$$

The terms of the cross-sectional stiffness matrix in Eq. (42) would undergo significant reduction as damage evolves along the length of the beam. As the damage parameter modifies the local material property, the two-dimensional cross-sectional analysis would be repeated after each load increment for the beam elements to determine the degraded values of the stiffness coefficients. The flow chart in Fig. 5 summarizes the incremental procedure adopted to determine the effective properties for the re-entrant type geometry of the micro-structure as the damage evolves.

3. Results and discussion

In this section, the effect of damage evolution on the auxetic behavior of the two-dimensional (Fig. 2) and three-dimensional (Fig. 3) re-entrant geometries is investigated. For the numerical study dealing with the 2D re-entrant auxetic geometry, the length of the inclined
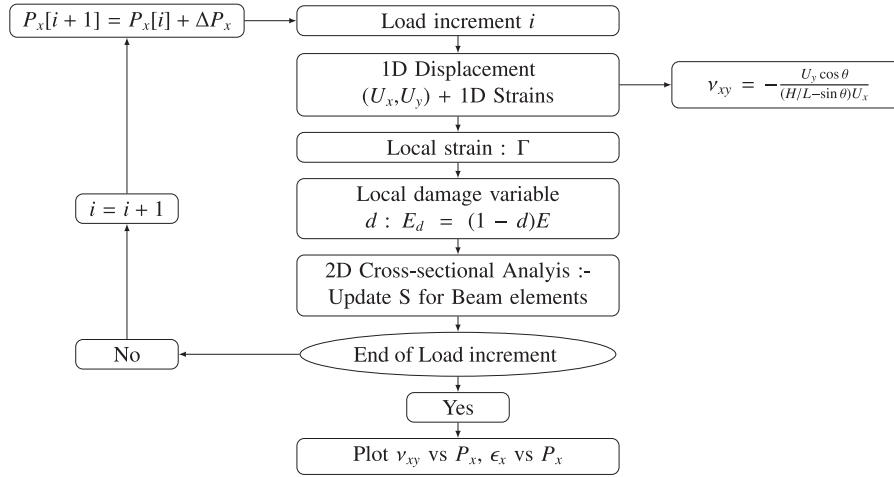
Fig. 5. Procedure for determining the effect of progressive damage evolution on the effective elastic properties for the 2D and 3D re-entrant geometry. At each load increment i, the local damage variable is evaluated as per the damage law from local strains. The modified material properties, i.e. E_d, are used to evaluate the modified cross-sectional stiffness for the beam element for the next load increment.

Table 1
Elastic properties for 2D and 3D re-entrant geometry from Euler–Bernoulli beam model ($L = 40$ mm; $\alpha = 2$, $k = 46$).

Model parameters		2D re-entrant		3D re-entrant	
α	θ	v_{xy}	E_x (kPa)	v_{zx}	E_z (kPa)
2	30°	−0.98	2160	−3.82	2450
2	40°	−0.66	1270	−2.24	992
2	50°	−0.43	827	−1.46	545
2	60°	−0.25	550	−0.98	370

member AB (ref. Fig. 2) is assumed to be 40 mm. Further, the cross-section for the beam is considered to be square-shaped with a thickness of 3 mm, such that the slenderness ratio for the inclined members, i.e. $k = 46$. The ratio of the length of the vertical strut to the inclined horizontal strut, i.e. $\alpha = 2$ and the material for the auxetic frame was taken to be ABS plastic, for which E = 2.2 GPa and $v = 0.37$ (Li et al., 2020). Based on the small deformation theory [ref. Eqs. (5) and (6)], the magnitude of the Poisson's ratio (v_{xy}) and effective elastic modulus (E_x) for the 2D re-entrant geometry are tabulated in Table 1 for different values of the rib-inclination angle, i.e. θ. Considering the influence of different values of rib-inclination angles θ, it can be witnessed from the numerical results that with a higher value of rib-inclination angle, the Poisson's ratio becomes increasingly less negative, thereby indicating a reduction in the degree of auxetic behavior. Further, the assessment from the small deformation theory is extended to 3D re-entrant geometry. To this end, similar to the 2D geometry, the dimension for the member O_1E (Fig. 3) was assumed to be 40 mm, the cross-section for the beam is considered to be square-shaped with a thickness of 3 mm and the ratio of the length of the vertical strut to the inclined horizontal strut, i.e. $\alpha = 2$. The results from the Euler–Bernoulli beam model [ref. Eqs. (10) and (11)] tabulated in Table 1 for 3D re-entrant geometry with different values of θ reveal that the degree of auxeticity enhances as the value of θ, diminishes. (ref. Section 2).

3.1. Material behavior

The value of limiting strain for the linear elastic behavior of the material of the auxetic frame, i.e. ABS Plastic was considered to be 0.013 (Li et al., 2020; Hu et al., 2019). Acrylonitrile–butadiene–styrene (ABS) is a widely used amorphous thermoplastic, which exhibits minimal strain hardening (Hu et al., 2019). The tensile stress–strain behavior for the material is closer to ideal elastic plastic behavior shown in Fig. 6 (Dundar et al., 2021; Hu et al., 2019). Hence, the damage parameter d

was estimated as per the following damage law to represent the experimentally observed stress–strain behavior for ABS plastic in previous works (Einav et al., 2007; Hu et al., 2019):

$$d = 1 - \frac{\epsilon_o}{\Gamma_{11}}\pi(d) \qquad \Gamma_{11} > \epsilon_o \tag{46}$$

where, ϵ_o, is the damage initiation strain for the material (ref. Fig. 6), Γ_{11} is the local tensile strain determined from the recovery relations (Section 2.3) and $\pi(d) = 1$ for ideal elastic plastic behavior. The methodology adopted in the present work can also be extended to materials which exhibit plastic hardening after finite deformations. Previously, coupled damage and plasticity models have been developed (Einav et al., 2007), wherein, it was shown that the same constitutive framework can be adopted to describe both the growth of damage and the evolution of plastic strains, i.e. damage laws can be tailored to represent specific material behaviors such as plastic hardening ($\pi(d) > 1$) and softening ($\pi(d) < 1$) as shown in Fig. 6. Appropriate damage laws can be plugged into the variational asymptotic method based cross-sectional analysis to determine the change in cross-sectional bending stiffness and the resultant deformation characteristics of the constituting members of the auxetic frame to predict the change in macroscale mechanical behavior for the geometries.

3.2. Mesh convergence

As discussed in Section 2, one-dimensional non-linear beam analysis should be coupled with two-dimensional cross-sectional analysis to accurately predict the affect of local material degradation on the cross-sectional stiffness of the inclined members and the deformed configuration of the geometry. In this context a mesh convergence analysis was carried out for the finite element implementation of the variational asymptotic method based cross-sectional analysis (ref. Section 2.1) as well as for the 3D FEM simulations carried out in Abaqus (UMAT).

For the 3D FEM simulations and the VAM based methodology adopted in the present work, the half-length cantilever beam models (ref. Section 2) were employed to predict load-dependent behavior for the 2D and 3D geometry, wherein periodicity is imposed by suppressing joint rotations. The boundary conditions imposed on the half length beam representing the inclined members of the 2D and 3D re-entrant geometry are shown in Fig. 7(d). Previously the half-length cantilever beam models have been used to predict the strain-dependent behavior of the re-entrant geometries and the resultant numerical response under large deformations has also been experimentally validated (Wan et al., 2004; Yang et al., 2015; Srivastava et al., 2023a).
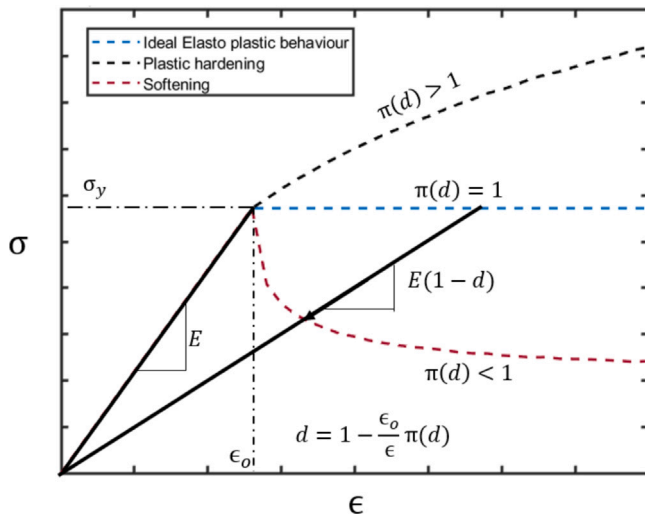
Fig. 6. (a) Strain vs. stress behavior of one-dimensional damage hyperelasticity model for ideal elasto plastic behavior, plastic hardening and softening (Einav et al., 2007).

Fig. 7 shows the variation of strain determined as per Eq. (2) from the deformed configuration, i.e. the tip deflections of the cantilever for the 2D re-entrant geometry ($\theta = 30°$, $\alpha = 2$) with applied tensile loads. Fig. 7(a) shows the change in the mechanical behavior for the geometry with damage progression as predicted by the 3D FEM simulations, wherein the damage law was implemented using UMAT for varying cross-sectional mesh sizes, i.e. 2×2, 4×4 and 8×8 mesh of the beam (ref. Fig. 7(c)). The results for the 4×4 and 8×8 mesh sizes converge well, indicating that the results do not vary for increasing mesh refinements in Abaqus. Similarly, Fig. 7(b) shows the strain vs load behavior as determined from the VAM and GEBT based methodology adopted in the present work for different mesh sizes compared against the converged results from the 3D FEM simulations, wherein it is observed that the results for 4×4 and 8×8 mesh sizes are sufficiently convergent. Hence, the square shaped cross-section of the inclined members of the 2D and 3D re-entrant geometries was sub-divided into 16 elements (4×4 mesh) for the finite element implementation of the VAM based cross-sectional analysis in the present work, whereas for the one-dimensional non-linear beam analysis (ref. Section 2.2), the beam was discretized into 19 elements along the length as shown in Fig. 7(d).

3.3. Cross-sectional analysis accounting for damage

The terms of the cross-sectional stiffness matrix are a function of geometric and material parameters, and hence would undergo significant reduction as the material in the cross-section degrades. As shown in Fig. 8, the flexural rigidity or bending stiffness (Fig. 2) as determined from the methodology based on VAM and GEBT (Section 2) for the cross-section at the root of the half-length cantilever beam AO (ref. Fig. 2) for the 2D re-entrant geometry ($\alpha = 2$, $\theta = 30°$) decreases with increasing magnitudes of normalized compressive load, i.e. P_x/P_{cr}, where, P_{cr}, is the critical buckling load for the half length cantilever beam. Fig. 8 also shows contour plots for the damage parameter d over the cross-section for different values of applied load, wherein the damage parameter varies between 0 to 1.

As emphasized in Section 2.3, the damage parameter is determined from the evolution of the local strain at the material points. It can be inferred from the contour plots that initially for lower magnitudes of applied loads, the cross-section remains relatively undamaged (i.e. $P_x/P_{cr} = -0.23$), however, as the magnitude of the applied far-field stress increases, the cross-section damages significantly (i.e. $P_x/P_{cr} = -0.33$). Since the damage is driven by tensile strain, the damage is more

predominant over the half of the cross-section under tension as the member AB exhibits a bending dominant mode of deformation. Due to progressive reduction in flexural stiffness, the deformed configuration of the geometry is affected significantly, thereby implying a corresponding impact on the macroscale behavior of the auxetic geometry.

3.4. Load vs. strain behavior

For a 2D re-entrant geometry (Fig. 2), the variation of the macroscale strain (ϵ_x) with normalized compressive and tensile load (P_x/P_{cr}) for rib-inclination angle, i.e. $\theta = 30°$ is plotted in Fig. 9(a) along with the deformed configuration of the geometry under compression. The macroscale strain (ϵ_x) has been determined from the geometry's deformed configuration as per Eq. (2). The results from the 2D cross-sectional analysis and 1D non-linear beam analysis in the present work (Fig. 5) have been compared and verified against the results from Abaqus (v6.17) wherein, the damage law was implemented through user material subroutine, UMAT. The slope of the load vs. strain plots indicates a marked degradation in the macroscale value of effective elastic modulus or stiffness in the x-direction (E_x). This is a consequence of increased deformations of the damaged members due to material non-linearity ($0 < d < 1$) as compared to the scenario, wherein damage is not considered ($d = 0$) (shown in Fig. 9(a)).

Fig. 9(b) also shows the 3D contour plots for the damage variable, i.e. d along the length of the half-length cantilever member AO at different values of the applied compressive load. From Fig. 9(b), it can be inferred that the damage is more predominant near the joints of the re-entrant geometry (ref. Fig. 2) and remains limited to the portion of the beam under tension. Previously Hu et al. (2019) fabricated and tested specimens for re-entrant anti-trichiral honeycombs, wherein plastic hinges formed near the joints of the microstructure due to the elastic plastic behavior of the base material, i.e. ABS, significantly affected mechanical response under large deformations, similar to the observation in the present work.

Fig. 10 shows the variation of macro-scale strain (ϵ_z) with applied compressive and tensile load in the vertical direction, i.e. P_z for the 3D re-entrant geometry, as well as the deformed configuration of the geometry under tension. The deformed configuration shows the increased deformation of the damaged members ($0 < d < 1$), relative to the undamaged members ($d = 0$). As in the case of 2D geometry, increased deformations of the damaged members, indicate a degradation in macro-scale effective elastic modulus.

The load vs strain behavior for the 2D and 3D geometry as determined from the methodology adopted in the present work is also compared against the elastica model presented by Wan et al. (2004) as shown in Figs. 9 and 10. The elastica theory, similar to the Euler–Bernoulli beam model neglects cross-sectional warping, i.e. flexural rigidity is independent of the curvature along the beam reference line as well as the material degradation, hence the load-dependent behavior as predicted by the elastic model agrees well with the undamaged results ($d = 0$).

3.5. Quantification of the Young's modulus and the Poisson's ratio with damage evolution

In order to quantify the effect of damage on the effective elastic properties of the material, certain indices are introduced in this section. The effect of material degradation on the effective elastic modulus of the geometry is quantified by the parameter η defined as follows:

$$\eta = \left| \frac{E_{UD} - E_D}{E_{UD}} \right| \times 100\% \tag{47}$$

where E_{UD} is the value of the undamaged effective elastic modulus. In other words, the effective elastic modulus E_{UD} is obtained by considering only the effect of geometric non-linearity or large deflections of the
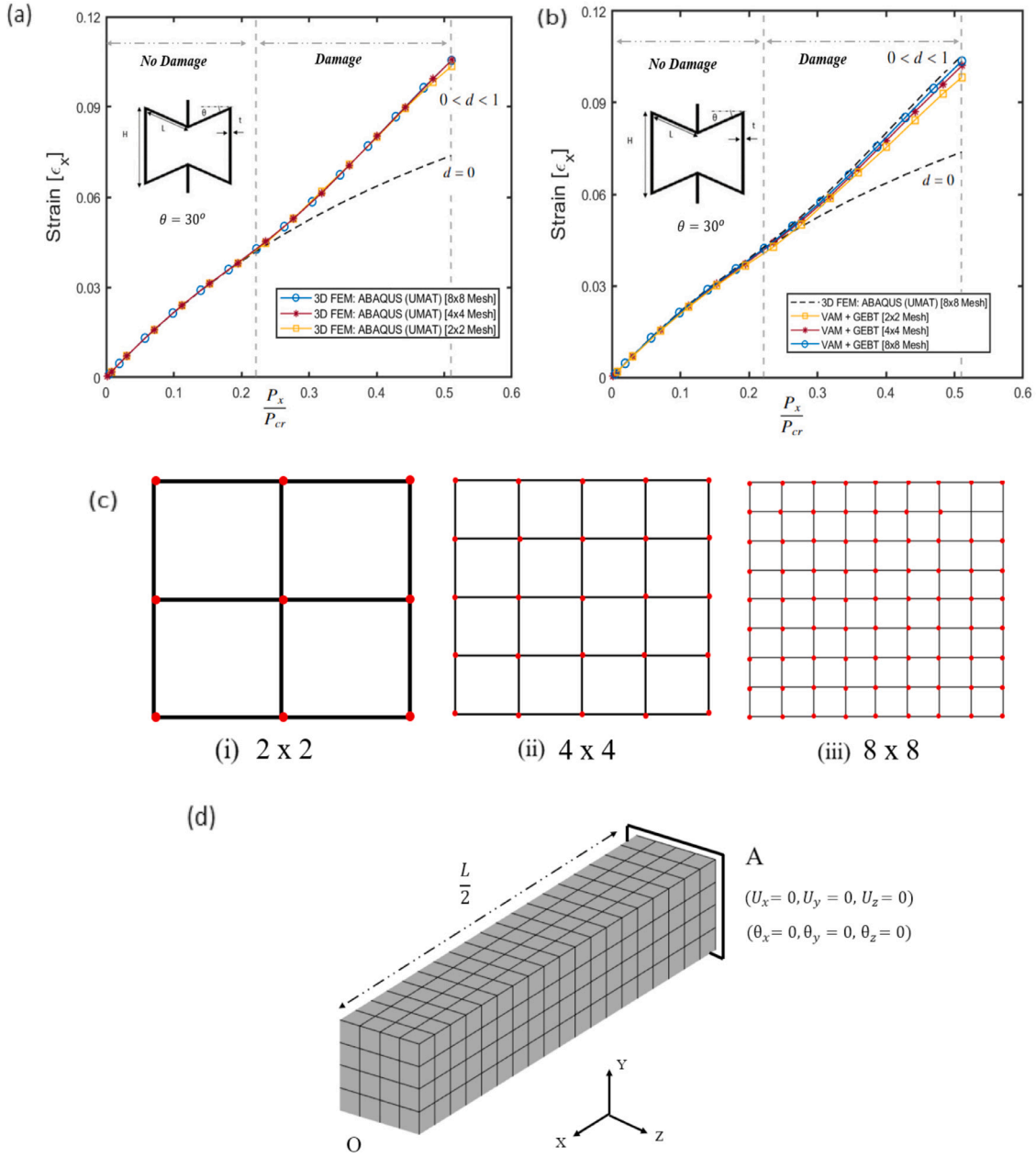
Fig. 7. (a) Strain vs. applied load behavior for 2D re-entrant geometry ($\theta = 30°$, $\alpha = 2$) plotted for varying cross-sectional mesh sizes in Abaqus (UMAT) (b) Strain vs. applied load behavior for 2D re-entrant geometry ($\theta = 30°$, $\alpha = 2$) plotted for varying cross-sectional mesh sizes adopted for two-dimensional cross-sectional analysis (VAM) in the present work. (c) Varying mesh sizes considered in the present work for convergence analysis [2 × 2, 4 × 4 and 8 × 8] (d) Finite element mesh adopted for the half length cantilever beam models for 2D and 3D re-entrant geometries (Wan et al., 2004; Yang et al., 2015) in 3D FEM (Abaqus) simulations and present work (VAM + GEBT).

constituting members of the geometry. Meanwhile, E_D is the value of effective elastic modulus determined by taking into account the effect of material degradation as well. Similarly, in order to quantify the effect of damage on Poisson's ratio, the parameter β is introduced:

$$\beta = \left| \frac{v_D - v_{UD}}{v_{UD}} \right| \times 100\% \qquad (48)$$

where v_{UD} is the value of Poisson's ratio considering the material of the auxetic frame to be undamaged and v_D is the value of Poisson's ratio considering the effect of damage as well as large deformations. Therefore, higher values of the parameters η and β indicate a greater impact of material behavior on the effective elastic properties. To this end, a parametric study is conducted to analyze the effect of damage on the auxetic mechanical properties for various rib inclination angles of the 2D and 3D auxetic geometries.

Figs. 11(a–d) and 12(a–d) show the variation of Poisson's ratio, (v_{xy}) and effective elastic modulus (E_x) with applied tensile and compressive loads respectively for the 2D auxetic frame for various rib inclination angles. The results are compared with the scenario, wherein the effect of damage is not considered ($d = 0$), i.e. considering only the effect of geometric non-linearity or large deflections of the members constituting the geometry. It can be inferred that under the effect of tensile and compressive loads, the value of Poisson's ratio deviates significantly from the values predicted by small-deformation theory (ref. Table 1). Further, as the effect of damage along the length of the member AO becomes more pronounced, the value of Poisson's ratio diverges significantly from the values obtained for undamaged material, i.e. the parameter β increases as v_D becomes increasingly more negative compared to v_{UD} under tension (ref. Fig. 11) and increasingly less negative under compression (ref. Fig. 12). Similarly, the effective
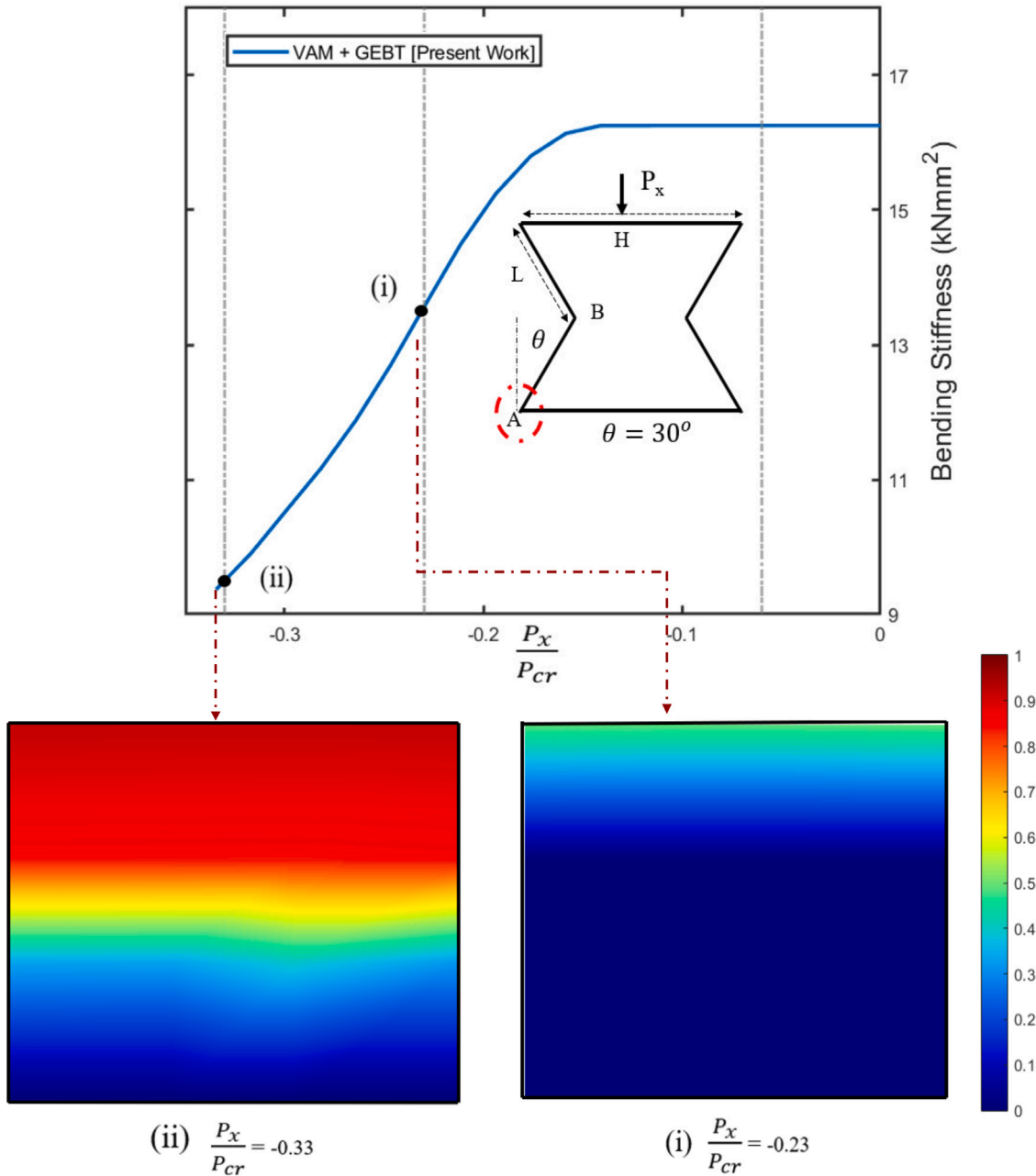
Fig. 8. Variation of bending stiffness for the cross-section at joint A of the member A0 (ref. Fig. 2) as determined from the methodology based on VAM and GEBT (Section 2) and 2D contour plots for the damage variable, i.e. d at different values of applied loads ($P_x/P_{cr} = -0.23$ and $P_x/P_{cr} = -0.33$) for the cross-section.

elastic modulus deviates significantly from the corresponding values predicted by small deformation theory (ref. Table 1), and as damage progresses along the length of the members, deviation from the values obtained for undamaged material is observed, i.e. the value of the index η increases as E_D becomes increasingly less compared to E_{UD} under tension as well as compression.

Figs. 13(a–d) and 14(a–d) show the variation of Poisson's ratio (ν_{zx}), and effective elastic modulus (E_z) with applied tensile and compressive loads respectively for the 3D auxetic frame for various rib inclination angles. Similar to the 2D geometry, as the effect of damage along the length of the member O_1E becomes more pronounced, the value of Poisson's ratio diverges significantly from the values obtained for undamaged material, i.e. the parameter β increases as ν_D becomes increasingly less negative compared to ν_{UD} under tension (ref. Fig. 13)

and increasingly more negative under compression (ref. Fig. 14). Similarly, for the effective elastic modulus (E_z) the value of the parameter η increases, indicating a rapid degradation in macroscale stiffness for the 3D re-entrant geometry under tension as well as compression It is also observed that the range of applied tensile load over which the effect of damage is not significant, i.e. $\eta = 0$ and $\beta = 0$, is inversely related to rib-inclination angle for the 2D and the 3D re-entrant geometry.

4. Conclusions

In this article, the influence of damage on the auxetic behavior of 2D and 3D re-entrant geometries has been investigated using the variational asymptotic method in a geometrically nonlinear framework. The proposed methodology incorporates the two-dimensional cross-sectional analysis and geometrically exact one-dimensional beam
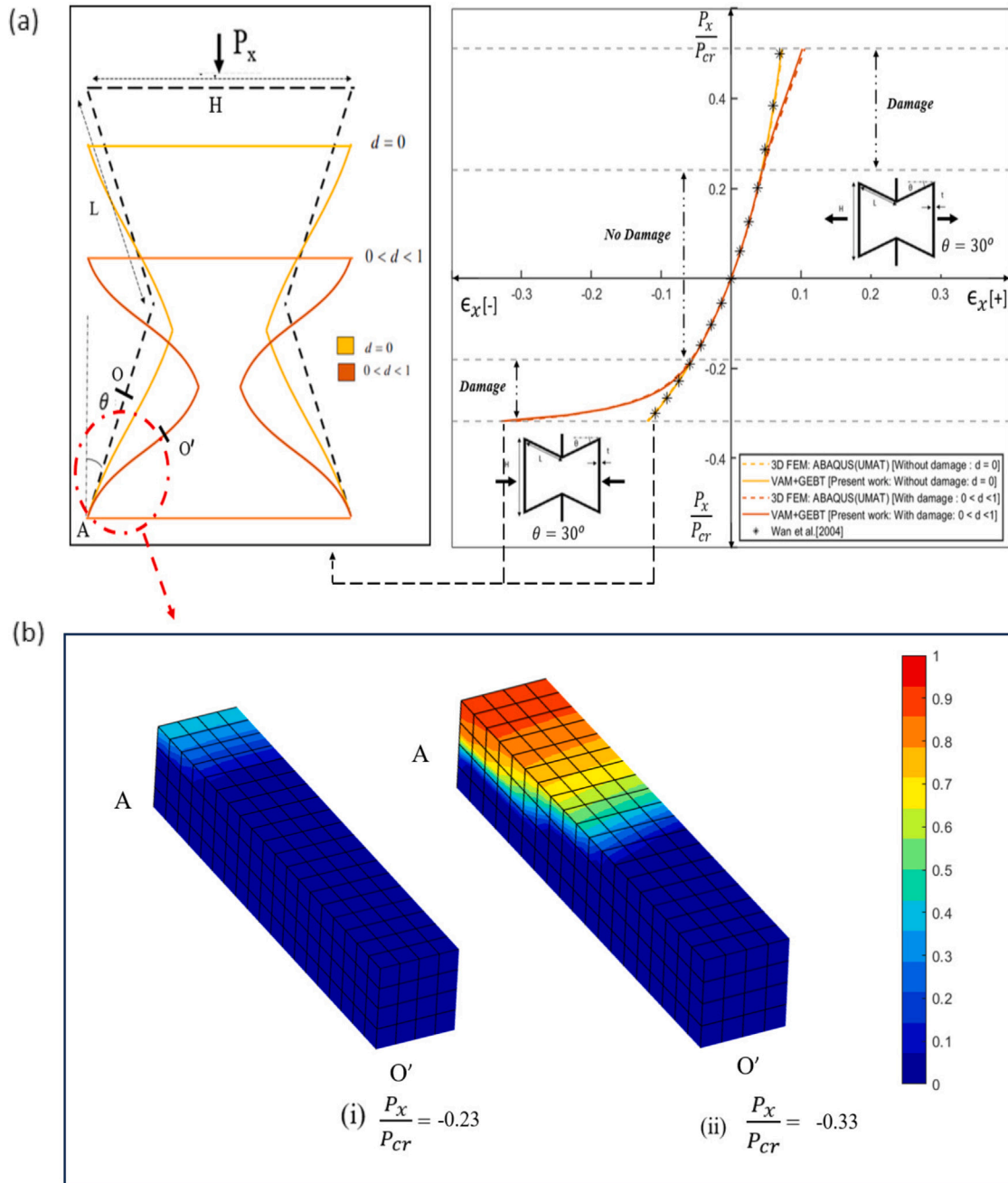
Fig. 9. (a) Variation of strain (ϵ_x) with applied compressive and tensile load, i.e. P_x, and the deformed configuration of the 2D re-entrant geometry for $\theta = 30°$ as determined from the methodology based on (VAM + GEBT), verified with results from 3D FEM [Abaqus (UMAT)]. (b) 3D contour plot for the damage variable d for the inclined half-length member A0 [ref. Fig. 2] at different values of applied loads ($P_x/P_{cr} = -0.23$ and $P_x/P_{cr} = -0.33$).

theory to capture the degradation of cross-sectional stiffness of auxetic members using an isotropic damage law. The resulting numerical framework, implemented in an in-house Python code, was employed to quantify the effect of material degradation on the macroscale effective elastic modulus and Poisson's ratio of the re-entrant type geometry. The results obtained from the proposed formulation were verified with the 3D finite element results obtained using the FEM tool, Abaqus together with a user subroutine UMAT to model damage evolution. The numerical evaluation suggests that the macroscale behavior of the re-entrant geometries was significantly affected by the damage progression. The value of effective modulus was considerably reduced under tensile and compressive far-field stresses for the 2D and 3D microstructures. Under tension, the auxetic behavior improved slightly

for the 2D re-entrant geometry due to increased deformations, while in the case of the 3D re-entrant geometry, the value of Poisson's ratio became less negative for the damaged material. Under compression the auxetic behavior improved for the 3D configuration, while in the case of the 2D re-entrant geometry, the value of Poisson's ratio became less negative. It was also observed that the range of applied tensile and compressive loads over which the effect of damage is not significant is inversely related to the rib-inclination angle for the 2D and 3D geometries respectively. Thus, the numerical examples in this work indicate that physical non-linearity arising due to material degradation should be accounted for when it comes to the analysis and design of auxetic materials for structural applications.
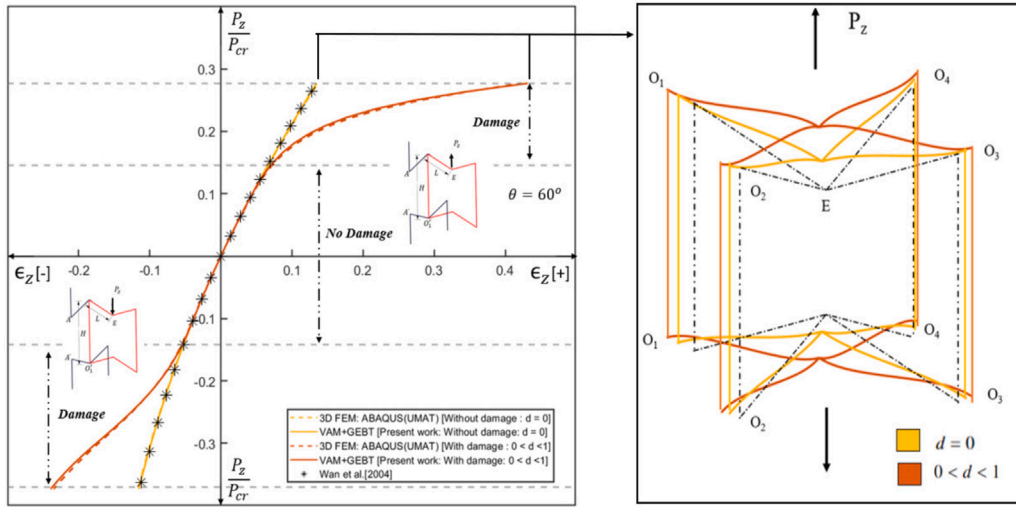
Fig. 10. (a) Variation of strain (ϵ_z) with applied compressive and tensile load, i.e. P_z, and the deformed configuration of the 3D re-entrant geometry for $\theta = 60°$ as determined from the methodology based on VAM and GEBT verified with results from 3D FEM [Abaqus(UMAT)].
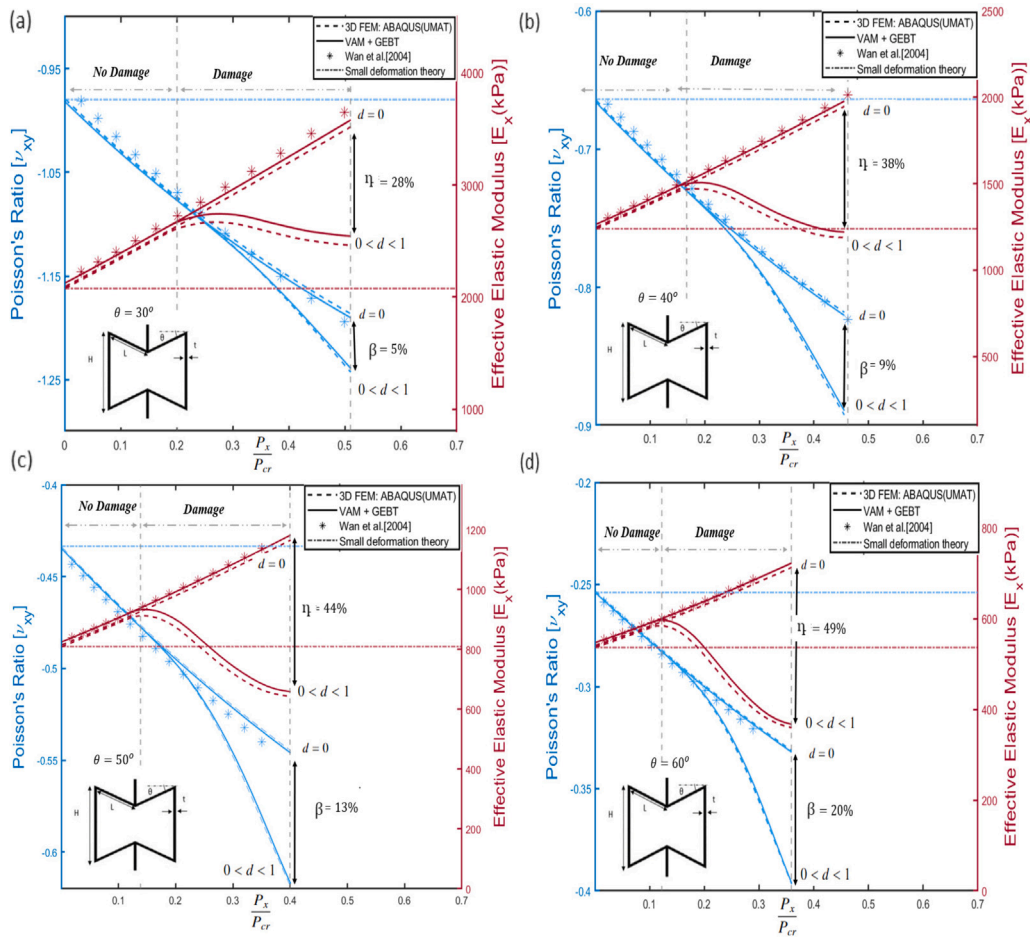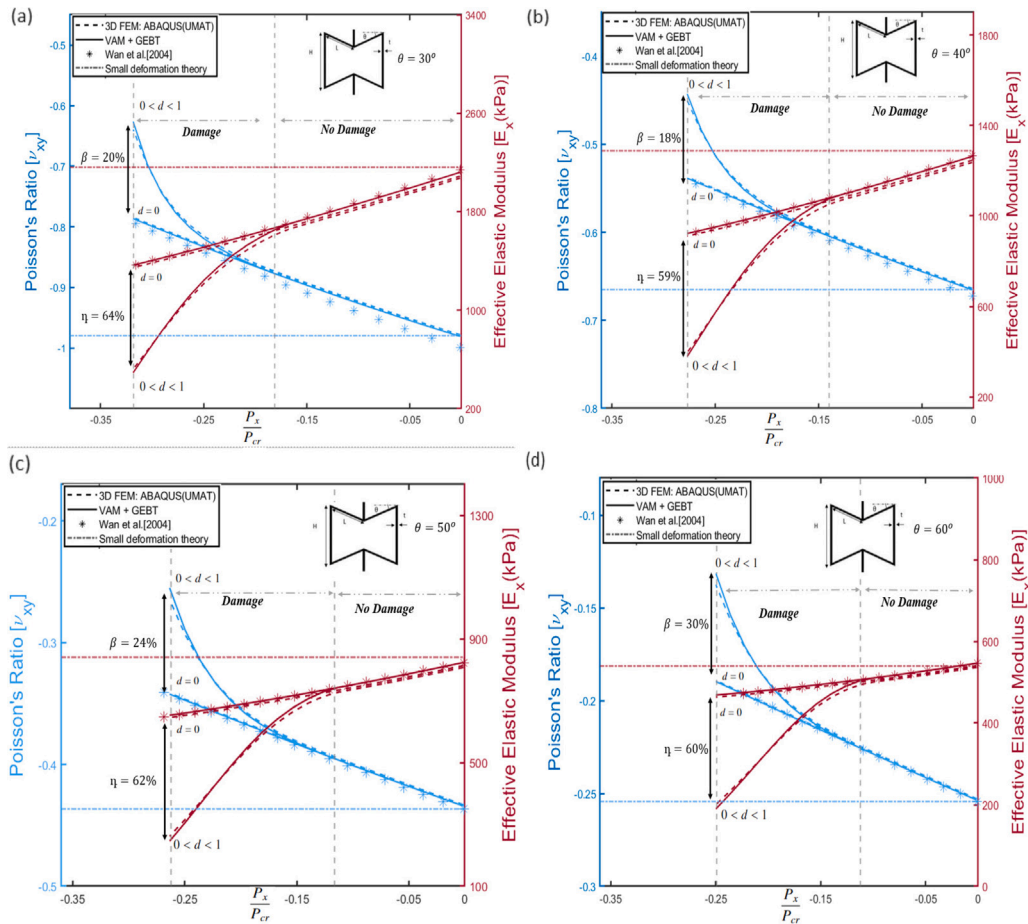

Fig. 11. Variation of Poisson's ratio, i.e. ν_{xy} and effective elastic modulus, i.e. E_x with applied tensile load in the horizontal direction, i.e. P_x/P_{cr} for different rib inclination angles for the 2D re-entrant geometry: (a) $\theta = 30°$, (b) $\theta = 40°$, (c) $\theta = 50°$ and (d) $\theta = 60°$. The results from the methodology based on (VAM + GEBT), are verified with results from 3D FEM [Abaqus (UMAT)]. The effect of damage evolution on elastic properties is quantified by the parameters η and β, for effective elastic modulus and Poisson's ratio respectively.

Fig. 12. Variation of Poisson's ratio, i.e. v_{xy} and effective elastic modulus, i.e. E_x with applied compressive load in the horizontal direction, i.e. P_x/P_{cr} for different rib inclination angles for the 2D re-entrant geometry: (a) $\theta = 30°$, (b) $\theta = 40°$, (c) $\theta = 50°$ and (d) $\theta = 60°$. The results from the methodology based on (VAM + GEBT), are verified with results from 3D FEM [Abaqus (UMAT)]. The effect of damage evolution on elastic properties is quantified by the parameters η and β, for effective elastic modulus and Poisson's ratio respectively.

CRediT authorship contribution statement

Chetna Srivastava: Investigation, Methodology, Writing – original draft, Data curation, Software, Validation, Visualization. **Vinyas Mahesh:** Supervision, Writing – review & editing. **P.J. Guruprasad:** Supervision, Writing – review & editing. **Nik Petrinic:** Writing – review & editing. **Fabrizio Scarpa:** Writing – review & editing. **Dineshkumar Harursampath:** Supervision, Writing – review & editing, Project administration. **Sathiskumar A. Ponnusami:** Conceptualization, Supervision, Writing – review & editing, Project administration.

Declaration of competing interest

Data availability

Data will be made available on request.

Appendix A

In this section the detailed mathematical formulations for the two-dimensional cross-sectional analysis and one-dimensional beam analysis (ref. Section 2) as adopted from the work by Hodges (2006) has been presented:

A.1. 2D cross-sectional analysis

As shown in Fig. 4, the position vector ($\hat{\boldsymbol{r}}$) to any material point on the undeformed cross-section of the beam is expressed in terms of the measure numbers along $\boldsymbol{b_1}$, $\boldsymbol{b_2}$ and $\boldsymbol{b_3}$ i.e.,

$$\hat{\boldsymbol{r}}(x_1, x_2, x_3) = x_1 \boldsymbol{b_1} + x_2 \boldsymbol{b_2}(x_1) + x_3 \boldsymbol{b_3}(x_1) \tag{A.1}$$

where, x_1 is measured along the beam reference line and x_2, x_3 are measure numbers along $\boldsymbol{b_2}$ and $\boldsymbol{b_3}$.

Similarly, the position vector of a material point in the deformed cross-section ($\hat{\boldsymbol{R}}$) is expressed as follows (ref. Section 2.1.1):

$$\hat{\boldsymbol{R}} = \boldsymbol{r} + \boldsymbol{u} + x_2 \boldsymbol{B_2} + x_3 \boldsymbol{B_3} + w_i \boldsymbol{B_i} \tag{A.2}$$

From the definition of covariant and contravariant vectors, the deformation gradient tensor $\underline{\boldsymbol{X}}$ is given by :

$$\underline{\boldsymbol{X}} = \boldsymbol{G_i} \boldsymbol{g^i} \tag{A.3}$$

where

$$\boldsymbol{g^i} = \frac{\epsilon_{ijk}}{2\sqrt{g}} \boldsymbol{g_j} \times \boldsymbol{g_k} \tag{A.4}$$

$$\boldsymbol{g_1} = \frac{\partial \hat{\boldsymbol{r}}}{\partial x_1} \qquad \boldsymbol{g_2} = \frac{\partial \hat{\boldsymbol{r}}}{\partial x_2} \qquad \boldsymbol{g_3} = \frac{\partial \hat{\boldsymbol{r}}}{\partial x_3} \tag{A.5}$$

$$\boldsymbol{G_1} = \frac{\partial \hat{\boldsymbol{R}}}{\partial x_1} \qquad \boldsymbol{G_2} = \frac{\partial \hat{\boldsymbol{R}}}{\partial x_2} \qquad \boldsymbol{G_3} = \frac{\partial \hat{\boldsymbol{R}}}{\partial x_3} \tag{A.6}$$
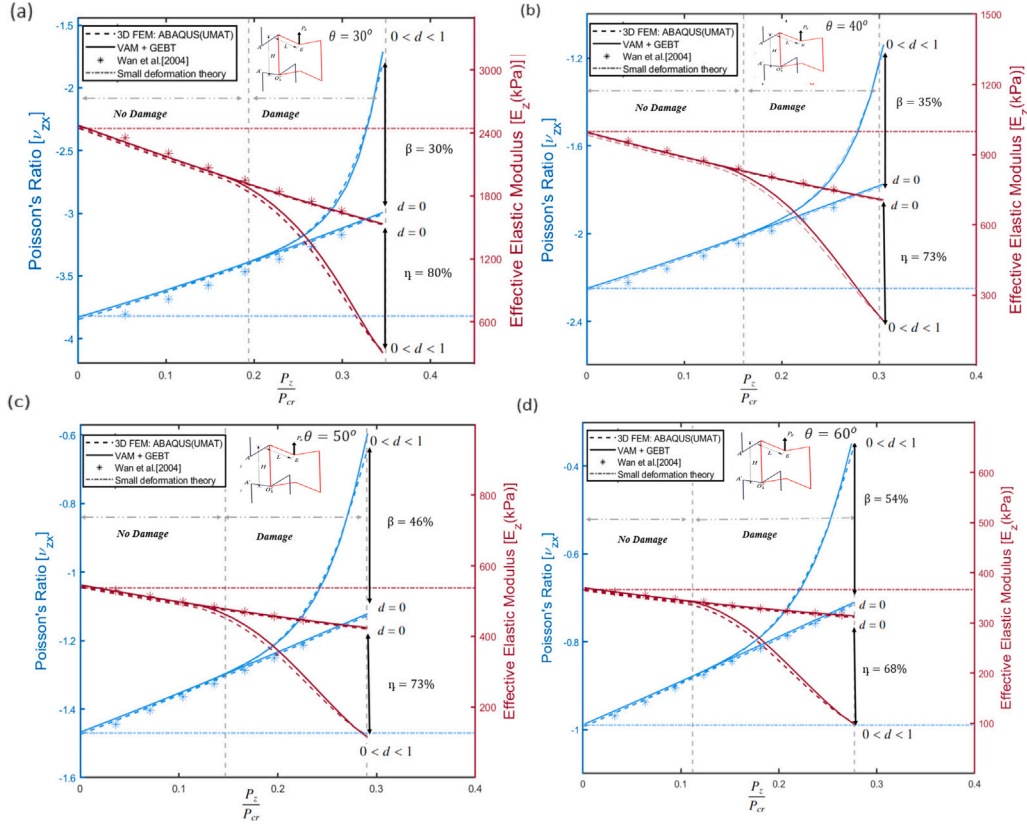
Fig. 13. Variation of Poisson's ratio, i.e. v_{zx} and effective elastic modulus, i.e. E_z with applied tensile load in the vertical direction, i.e. P_z/P_{cr} for different rib inclination angles for the 3D re-entrant geometry: (a) $\theta = 30°$, (b) $\theta = 40°$, (c) $\theta = 50°$ and (d) $\theta = 60°$. The results from the methodology based on (VAM + GEBT), are verified with results from 3D FEM [Abaqus (UMAT)]. The effect of damage evolution on elastic properties is quantified by the parameters η and β, for effective elastic modulus and Poisson's ratio respectively.

In Eq. (A.4), $\sqrt{g} = det(g_i.g_j)$, substituting Eq. (A.1) in Eq. (A.5), we have the following equations for the covariant vectors:

$$g_1 = (1 - x_2k_3 + x_3k_2)b_1 + k_1x_2b_2 - k_1x_3b_3 \tag{A.7}$$

$$g_2 = b_2 \tag{A.8}$$

$$g_3 = b_3 \tag{A.9}$$

With reference to Eq. (14), k_i are the measure numbers for the initial curvature of the beam in the b_i basis, i.e. k_1 is the pretwist along the beam reference line, and k_1 and k_2 are the initial curvatures about b_2 and b_3. Substituting Eqs. (A.7), (A.8) and (A.9) in Eq. (A.4), the contra-variant vectors are determined as follows:

$$g^1 = \frac{b_1}{\sqrt{g}} \tag{A.10}$$

$$g^2 = \frac{x_3k_1}{\sqrt{g}}b_1 + b_2 \tag{A.11}$$

$$g^3 = -\frac{x_2k_1}{\sqrt{g}}b_1 + b_3 \tag{A.12}$$

where $\sqrt{g} = 1 - x_2k_3 + x_3k_2$, further in the deformed configuration of the beam the B_1 vector, is not tangential to the deformed center-line. Considering the T_i triad, the position vector to a material point can be re-expressed as follows:

$$\hat{R} = r + u + x_2T_2 + x_3T_3 + \bar{w}_iT_i \tag{A.13}$$

From Eq. (25), it can be inferred that in the T_i basis, shear deformation is considered to be a part of the warping field $\bar{w}_i$. The deformation gradient tensor components, in the mixed basis is expressed as follows:

$$X_{ij} = T_i.G_kg^k.b_j \tag{A.14}$$

where, the covariant vectors for the deformed configuration are determined by substituting Eq. (A.13) in Eq. (A.6):

$$G_1 = (1 + \bar{\gamma}_{11} - x_2K_3 + x_3K_2 - w_2K_3 + w_3K_2 + w_{1,1})T_1$$
$$+ (-x_3K_1 + w_1K_3 - w_3K_1 + w_{2,1})T_2$$
$$+ (x_2K_1 - w_1K_2 + w_2K_1 + w_{3,1})T_3$$

$$G_2 = T_2 + w_{1,2}T_1 + w_{2,2}T_2 + w_{3,2}T_3$$

$$G_3 = T_3 + w_{1,3}T_1 + w_{2,3}T_2 + w_{3,3}T_3$$

The terms of the deformation gradient tensor are determined from Eq. (A.14) as follows:

$$X_{11} = \frac{1 + \bar{\gamma}_{11} - x_2K_3 + x_3K_2 - w_2K_3 + w_3K_2 + w_{1,1}}{\sqrt{g}} + \frac{x_3k_1w_{1,2}}{\sqrt{g}}$$
$$- \frac{x_2k_1w_{1,3}}{\sqrt{g}}$$

$$X_{12} = w_{1,2}$$

$$X_{13} = w_{1,3}$$

$$X_{22} = 1 + w_{2,2}$$

$$X_{21} = \frac{-x_3K_1 + w_1K_3 - w_3K_1 + w_{2,1}}{\sqrt{g}} + \frac{(1 + w_{2,2})x_3k_1}{\sqrt{g}} - \frac{w_{2,3}x_2k_1}{\sqrt{g}}$$

$$X_{23} = w_{2,3}$$

$$X_{33} = 1 + w_{3,3}$$

$$X_{32} = w_{3,2}$$

$$X_{31} = \frac{x_2K_1 - w_1K_2 + w_2K_1 + w_{3,1}}{\sqrt{g}} + \frac{w_{3,2}x_3k_1}{\sqrt{g}} - \frac{(1 + w_{3,3})x_2k_1}{\sqrt{g}} \tag{A.15}$$
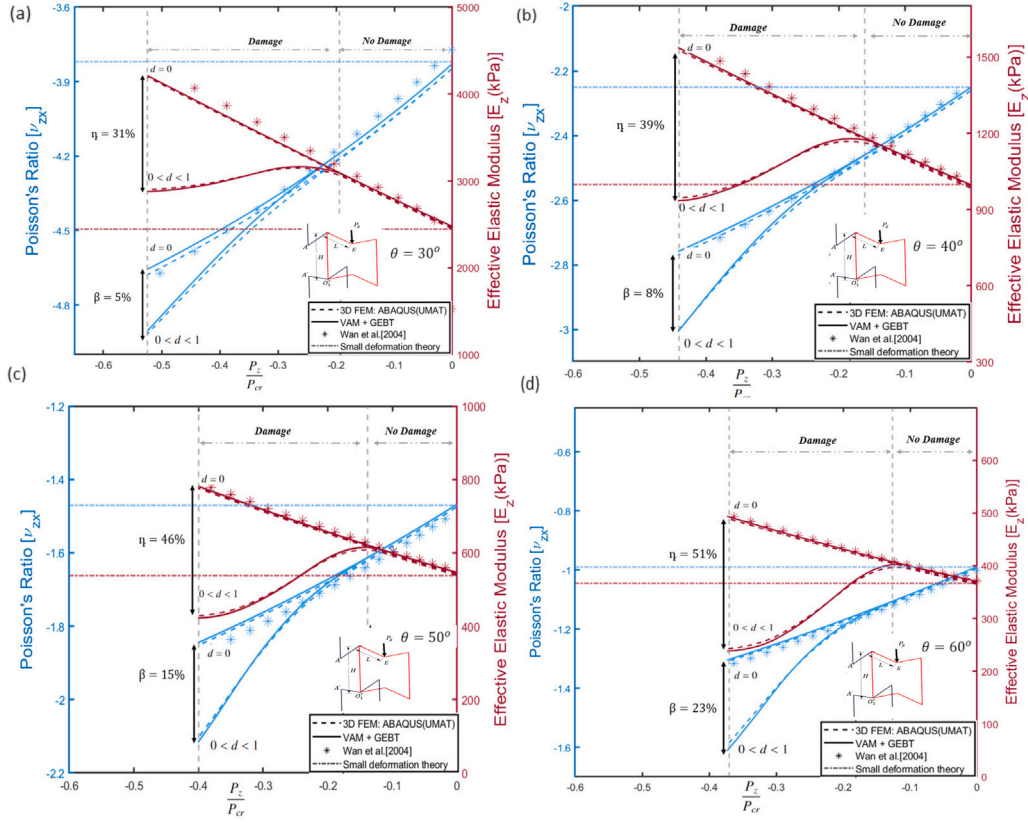
Fig. 14. Variation of Poisson's ratio, i.e. ν_{zx} and effective elastic modulus, i.e. E_z with applied compressive load in the vertical direction, i.e. P_z/P_{cr} for different rib inclination angles for the 3D re-entrant geometry: (a) $\theta = 30°$, (b) $\theta = 40°$, (c) $\theta = 50°$ and (d) $\theta = 60°$. The results from the methodology based on (VAM + GEBT), are verified with results from 3D FEM [Abaqus (UMAT)]. The effect of damage evolution on elastic properties is quantified by the parameters η and β, for effective elastic modulus and Poisson's ratio respectively.

$$\Gamma_{11} = \frac{\overline{\gamma}_{11} - x_2\overline{\kappa}_3 + x_3\overline{\kappa}_2 - w_2(k_3 + \overline{\kappa}_3) + w_3(k_2 + \overline{\kappa}_2) + w_{1,1} + x_3k_1w_{1,2} - x_2k_1w_{1,3}}{\sqrt{g}}$$

$$\Gamma_{22} = w_{2,2}$$

$$\Gamma_{33} = w_{3,3}$$

$$2\Gamma_{23} = w_{2,3} + w_{3,2}$$

$$2\Gamma_{12} = \frac{w_{1,2}(1 - x_2k_3 + x_3k_2) - x_3(k_1 + \bar{k}_1) + w_1(k_3 + \bar{\kappa}_3) - w_3(k_1 + \bar{\kappa}_1) + w_{2,1} + (1 + w_{2,2})x_3k_1 - w_{2,3}x_2k_1}{\sqrt{g}}$$

$$2\Gamma_{13} = \frac{w_{1,3}(1 - x_2k_3 + x_3k_2) + x_2(k_1 + \bar{k}_1) - w_1(k_2 + \bar{\kappa}_2) + w_2(k_1 + \bar{\kappa}_1) + w_{3,1} + w_{3,2}x_3k_1 - (1 + w_{3,3})x_2k_1}{\sqrt{g}}$$

(A.16)

Box I.

The three-dimensional strain components are determined as per Eq. (31) from the terms of the deformation gradient tensor: see the Eq. (A.16) in Box I.

The three-dimensional strains, after discarding the product of one-dimensional strain and warping can be written in the following matrix form:

$$\Gamma = \Gamma_a w + \Gamma_\epsilon \bar{\epsilon} + \Gamma_R w + \Gamma_l w' \tag{A.17}$$

where $\Gamma = [\Gamma_{11} \; 2\Gamma_{12} \; 2\Gamma_{13} \; \Gamma_{22} \; 2\Gamma_{23} \; \Gamma_{33}]^T$ and :

$$\Gamma_R = \frac{1}{\sqrt{g}}\begin{bmatrix} k_1(x_3\frac{\partial}{\partial x_2} - x_2\frac{\partial}{\partial x_3}) & -k_3 & k_2 \\ k_3 & k_1(x_3\frac{\partial}{\partial x_2} - x_2\frac{\partial}{\partial x_3}) & -k_1 \\ -k_2 & k_1 & k_1(x_3\frac{\partial}{\partial x_2} - x_2\frac{\partial}{\partial x_3}) \\ 0 & 0 & 0 \\ 0 & 0 & 0 \\ 0 & 0 & 0 \end{bmatrix}$$

$$\Gamma_a = \begin{bmatrix} 0 & 0 & 0 \\ \frac{\partial}{\partial x_2} & 0 & 0 \\ \frac{\partial}{\partial x_3} & 0 & 0 \\ 0 & \frac{\partial}{\partial x_2} & 0 \\ 0 & \frac{\partial}{\partial x_3} & \frac{\partial}{\partial x_2} \\ 0 & 0 & \frac{\partial}{\partial x_3} \end{bmatrix}$$

$$\Gamma_\epsilon = \frac{1}{\sqrt{g}} \begin{bmatrix} 1 & 0 & x_3 & -x_2 \\ 0 & -x_3 & 0 & 0 \\ 0 & x_2 & 0 & 0 \\ 0 & 0 & 0 & 0 \\ 0 & 0 & 0 & 0 \\ 0 & 0 & 0 & 0 \end{bmatrix} \quad \Gamma_l = \frac{1}{\sqrt{g}} \begin{bmatrix} 1 & 0 & 0 \\ 0 & 1 & 0 \\ 0 & 0 & 1 \\ 0 & 0 & 0 \\ 0 & 0 & 0 \\ 0 & 0 & 0 \end{bmatrix} \tag{A.18}$$

For a finite element implementation, the warping field is discretized (ref. Eq. (35)) and substituted in Eq. (36):

$$2U = V^T EV + 2V^T (D_{aR}V + D_{ae}\bar{\epsilon} + D_{aL}V') + V^T D_{RR}V + 2V^T D_{Re}\bar{\epsilon}$$
$$+ 2V^T D_{RL}V'$$
$$+ 2V'^T D_{Le}\bar{\epsilon} + V'^T D_{LL}V' + \bar{\epsilon}^T D_{\epsilon\epsilon}\bar{\epsilon} \tag{A.19}$$

where the coefficients are:

$$E = \int_A (\Gamma_a S)^T D \Gamma_a S . \sqrt{g} dx_2 dx_3$$

$$D_{aR} = \int_A (\Gamma_a S)^T D \Gamma_R S \sqrt{g} dx_2 dx_3$$

$$D_{ae} = \int_A (\Gamma_a S)^T D \Gamma_\epsilon \sqrt{g} dx_2 dx_3$$

$$D_{aL} = \int_A (\Gamma_a S)^T D \Gamma_L S \sqrt{g} dx_2 dx_3$$

$$D_{RR} = \int_A (\Gamma_R S)^T D \Gamma_R S \sqrt{g} dx_2 dx_3$$

$$D_{Re} = \int_A (\Gamma_R S)^T D \Gamma_\epsilon \sqrt{g} dx_2 dx_3$$

$$D_{RL} = \int_A (\Gamma_R S)^T D \Gamma_L S \sqrt{g} dx_2 dx_3$$

$$D_{Le} = \int_A (\Gamma_L S)^T D \Gamma_\epsilon \sqrt{g} dx_2 dx_3$$

$$D_{LL} = \int_A (\Gamma_L S)^T D \Gamma_L S \sqrt{g} dx_2 dx_3$$

$$D_{\epsilon\epsilon} = \int_A (\Gamma_\epsilon)^T D \Gamma_\epsilon \sqrt{g} dx_2 dx_3 \tag{A.20}$$

A.1.1. Zeroth order approximation

From the expression for strain energy i.e. Eq. (34), the zeroth order terms are retained, such that:

$$2U_0 = V^T EV + 2V^T D_{ae}\bar{\epsilon} + \bar{\epsilon}^T D_{\epsilon\epsilon}\bar{\epsilon} \tag{A.21}$$

The zeroth order strain energy functional is minimized subject to the constraint $\Gamma_a w = 0$, which for the discretized warping field can be written as follows:

$$V^T \int_A \Gamma_a S \sqrt{g} dx_2 dx_3 = 0$$
$$V^T D_c = 0$$

The Euler–Lagrange's equation for the minimization of the zeroth order strain energy function can be written as follows:

$$EV + D_{ae}\bar{\epsilon} = D_c \lambda \tag{A.22}$$

We know that for non-trivial solutions of the warping field, in order to satisfy the constraint $\Gamma_a w = 0$, the warping field should be of the following form (Hodges, 2006):

$$w_1 = c_1$$

$$w_2 = c_2 - c_4 x_3$$

$$w_3 = c_3 + c_4 x_2 \tag{A.23}$$

which implies that the matrix Γ_a has a kernel ψ:

$$\psi = \begin{bmatrix} 1 & 0 & 0 & 0 \\ 0 & 1 & 0 & -x_3 \\ 0 & 0 & 1 & x_2 \end{bmatrix} \tag{A.24}$$

The discretized kernel matrix can be written as $\psi = S\Psi$, such that the constraint on the warping field can be rewritten as $E\Psi = 0$, which allows for simplification for Lagrange's parameter by premultiplication with Ψ^T as follows:

$$\Psi^T EV + \Psi^T D_{ae}\bar{\epsilon} = \Psi^T D_c \lambda$$
$$\lambda = (\Psi^T D_c)^{-1} \Psi^T D_{ae}\bar{\epsilon} \tag{A.25}$$

The Lagrange's parameter vanishes since $\Psi^T D_{ae} = 0$, thereby implying that the Euler–Lagrange's equation is reduced to the following form:

$$EV = -D_{ae}\bar{\epsilon} \tag{A.26}$$

A.1.2. First order approximation

For the first-order solution, the warping field determined from the zeroth-order solution is perturbed as shown below:

$$V = V_o + V_1 \tag{A.27}$$

Retaining the leading terms, removing constant terms from zeroth order approximation and integrating by parts, the strain energy with the perturbed warping field is written as follows;

$$2U_1 = V_1^T EV_1 + 2V_1^T D_R \bar{\epsilon} + 2V_1^T D_S \bar{\epsilon}' \tag{A.28}$$

where,

$$D_R = D_{aR}\hat{V}_o + D_{aR}^T \hat{V}_o + D_{Re} \tag{A.29}$$

$$D_S = D_{aL}\hat{V}_o - D_{aL}^T \hat{V}_o - D_{Le} \tag{A.30}$$

Further, influence coefficients V_{1R} and V_{1S} are introduced such that:

$$V_1 = (V_{1R}\bar{\epsilon} + V_{1S}\bar{\epsilon}') \tag{A.31}$$

The Euler–Lagrange's equation for minimization of the strain energy functional subject to the constrain (Eq. (33)) can be written as follows :

$$EV_1 + D_R \bar{\epsilon} + D_S \bar{\epsilon}' = D_c \lambda \tag{A.32}$$

The Lagrange's parameter is solved for by pre-multiplication with Ψ^T

$$\lambda = (\Psi^T D_c)^{-1} \Psi^T (D_R \bar{\epsilon} + D_R \bar{\epsilon}') \tag{A.33}$$

Substituting in Lagrange's equation, we get :

$$EV_1 = \left[D_c (\Psi^T D_c)^{-1} \Psi^T - \Delta \right] (D_R \bar{\epsilon} + D_R \bar{\epsilon}') \tag{A.34}$$

The second-order asymptotically correct energy can be written as follows as presented as below:

$$2U_1 = \bar{\epsilon}^T A\bar{\epsilon} + \bar{\epsilon}^T B\bar{\epsilon}' + \bar{\epsilon}'^T C\bar{\epsilon}' + \bar{\epsilon}'^T D\bar{\epsilon}'' \tag{A.35}$$

where:

$$A = \hat{V}_o^T D_{ae} + D_{\epsilon\epsilon} + \hat{V}_o^T (D_{aR} + D_{aR}^T + D_{RR})\hat{V}_o + 2\hat{V}_o^T D_{Re} + V_{1R}^T D_R$$
$$B = \hat{V}_o^T (D_{al} + D_{Rl})\hat{V}_o + D_{le}^T \hat{V}_o + (\hat{V}_o^T D_{al} + D_{le}^T)V_{1R} + \frac{1}{2}(D_R^T V_{1S} + V_{1R}^T \bar{D}_S)$$
$$C = V_{1S}^T \bar{D}_S + \hat{V}_o^T D_{ll}\hat{V}_o$$
$$D = (\hat{V}_o^T D_{al} + D_{le}^T)V_{1S} \tag{A.36}$$

This expression for second-order asymptotically correct energy is converted to generalized Timoshenko form :

$$2U_1 = \epsilon^T X\epsilon + 2\epsilon^T Y\gamma_s + \gamma_s^T G\gamma_s \tag{A.37}$$

where,

$$G = (Q^T A^{-1}(C - B^T A^{-1} B) A^{-1} Q)^{-1}$$
$$Y = B^T A^{-1} Q G$$
$$X = A + Y G^{-1} Y^T \tag{A.38}$$

The 6×6 cross-sectional stiffness matrix can thereafter be determined as follows:

$$S = \begin{bmatrix} X & Y^T \\ Y & G \end{bmatrix} \tag{A.39}$$

Such that the one-dimensional strains can be related to force resultants as per the following equation:

$$\begin{bmatrix} F_1 \\ F_2 \\ F_3 \\ M_1 \\ M_2 \\ M_3 \end{bmatrix} = \begin{bmatrix} S_{11} & S_{12} & S_{13} & S_{14} & S_{15} & S_{16} \\ S_{12} & S_{22} & S_{23} & S_{24} & S_{25} & S_{26} \\ S_{13} & S_{23} & S_{33} & S_{34} & S_{35} & S_{36} \\ S_{14} & S_{24} & S_{34} & S_{44} & S_{45} & S_{46} \\ S_{15} & S_{25} & S_{35} & S_{45} & S_{55} & S_{56} \\ S_{16} & S_{26} & S_{36} & S_{46} & S_{56} & S_{66} \end{bmatrix} \begin{bmatrix} \gamma_{11} \\ 2\gamma_{12} \\ 2\gamma_{13} \\ \kappa_1 \\ \kappa_2 \\ \kappa_2 \end{bmatrix} \tag{A.40}$$

Appendix B

B.1. Geometrically exact beam theory

The equations for one-dimensional beam analysis are derived from extended Hamilton's principle:

$$\int_{t_1}^{t_2} \int_0^L \left[\delta(T - U) + \delta\bar{W} \right] = \delta\bar{A} \tag{B.1}$$

where T is the kinetic energy per unit length, U is the strain energy per unit length W is the virtual work done by the applied loads per unit length, A is the virtual action at the ends of the beam of length L, and t_1 and t_2, are arbitrary instances of time (Yu and Blair, 2012). For a static problem, the kinetic energy term is eliminated. The variation of the strain energy, which is a function of one-dimensional force and moment strains along the beam reference line, i.e. γ and κ can be written as follows:

$$\int_0^L \delta U dx_1 = \int_0^L \left[\delta\gamma^T \left(\frac{\partial U}{\partial \gamma} \right) + \delta\kappa^T \left(\frac{\partial U}{\partial \kappa} \right) \right] dx_1 \tag{B.2}$$

The partial derivative of the one-dimensional strain energy can be recognized as sectional force resultants, i.e.:

$$F = \left(\frac{\partial U}{\partial \gamma} \right) \qquad M = \left(\frac{\partial U}{\partial \kappa} \right) \tag{B.3}$$

where F is the column matrix with axial and shear forces and M is the column matrix with twisting and bending moments. Further, the variation of strain measures along the beam reference line are expressed as functions of virtual displacement and rotations, i.e. $\overline{\delta q}$ and $\overline{\delta \psi}$:

$$\delta\kappa = \overline{\delta\psi}' + \tilde{K}\overline{\delta\psi} \tag{B.4}$$
$$\delta\gamma = \overline{\delta q}' + \tilde{K}\overline{\delta q} + (\tilde{\gamma} + \tilde{e}_1)\overline{\delta\Psi} \tag{B.5}$$

where K is the curvature vector for the reference line of the deformed beam. Substituting the expressions for variation of strain measures in Eq. (B.2), the variation of strain energy can be written as follows:

$$\int_0^L \delta U dx_1 = \int_0^L \delta\gamma^T F + \delta^T M dx_1$$
$$= \int_0^L \left[(\overline{\delta q}')^T - \overline{\delta q}^T \tilde{K} - \overline{\delta\Psi}^T (\tilde{\gamma} \right.$$
$$\left. + \tilde{e}_1) \right] F + \left[(\overline{\delta\psi}')^T - \overline{\delta\psi}^T \tilde{K} \right] M dx_1$$

Substituting the above equation in Eq. (B.1):

$$\int_{t_1}^{t_2} \int_0^l \delta U - \delta W dx_1 dt = \int_{t_1}^{t_2} \int_0^l \left[(\overline{\delta q}')^T - \overline{\delta q}^T \tilde{K} - \overline{\delta\Psi}^T (\tilde{\gamma} + \tilde{e}_1) \right] F$$

$$+ \left[(\overline{\delta\psi}')^T - \overline{\delta\psi}^T \tilde{K} \right] M \tag{*}$$

$$- (\overline{\delta q})^T f - (\overline{\delta\psi})^T m dx_1 dt = \int_{t_1}^{t_2} (\overline{\delta q})^T \hat{F}$$

$$+ (\overline{\delta\psi})^T \hat{M}|_0^L dt \tag{B.6}$$

Eq. (B.6) is integrated by parts to get the following Euler–Lagrange equations:

$$F' + \tilde{K}F + f = 0$$
$$M + \tilde{K}M + m + (\tilde{\gamma} + \tilde{e}_1)F = 0$$

The above equations are used in conjunctions with kinematical equations and constitutive relations to determine the complete set of variables. Hodges (2006) presents the following mixed variational formulation for the one-dimensional beam equations, wherein the kinematical equations are added to the variational formulation. This involves constrained minimization of Hamilton's integral and determining the associated Lagrange's parameters:

$$\int_{t_1}^{t_2} \int_0^L \left\{ \left[(\overline{\delta q}')^T - \overline{\delta q}^T \tilde{K} - \overline{\delta\Psi}^T (\tilde{\gamma} + \tilde{e}_1) \right] F + \left[(\overline{\delta\psi}')^T - \overline{\delta\psi}^T \tilde{K} \right] M \right.$$

$$+ \delta\gamma^T \left[\left(\frac{\partial U}{\partial \gamma} \right)^T - F \right] + \delta\kappa^T \left[\left(\frac{\partial U}{\partial \kappa} \right)^T - M \right]$$

$$+ \overline{\delta F}^T \left[e_1 + \tilde{k}u - C^T(e_1 + \gamma) \right] - \left(\overline{\delta F}' \right)^T u$$

$$+ \overline{\delta M}^T \left[\Delta + \frac{\tilde{\theta}}{2} + \frac{\theta\theta^T}{4} \right] (Ck - k - \kappa)$$

$$\left. - \left(\overline{\delta M}' \right)^T \theta - (\overline{\delta q})^T f - (\overline{\delta\psi})^T m \right\} dx_1 dt$$

$$= \int_{t_1}^{t_2} (\overline{\delta q})^T \hat{F} + (\overline{\delta\psi})^T \hat{M} - \left(\overline{\delta F} \right)^T \hat{u} - \left(\overline{\delta M} \right)^T \hat{\theta} \Big|_0^L dt$$

where, C is the rotation matrix expressed in terms of the Rodrigues parameter θ (Hodges, 2006):

$$C = \frac{(1 - \frac{1}{4}\theta^T\theta)\Delta - \tilde{\theta} + \frac{1}{2}\theta\theta^T}{(1 + \frac{1}{4}\theta^T\theta)} \tag{B.7}$$

Yu and Blair (2012) present a general purpose finite element implementation for the above equation, wherein the following system of equations is solved for the discretized beam with N elements and N + 1 nodes:

At the starting node:

$$f_{u_1}^- - F_1^\star = 0 \quad f_{\psi_1}^- - M_1^\star = 0 \quad f_{F_1}^- - \hat{u}_1 = 0 \quad f_{M_1}^- - \hat{\theta}_1 = 0 \tag{B.8}$$

At the ending node:

$$f_{u_N}^+ - F_{N+1}^\star = 0 \quad f_{\psi_N}^+ - M_{N+1}^\star = 0 \quad f_{F_N}^+ - \hat{u}_{N+1} = 0 \quad f_{M_N}^+ - \hat{\theta}_{N+1} = 0 \tag{B.9}$$

At the intermediate node:

$$f_{u_i}^+ + f_{u_{i+1}}^- = 0 \quad f_{\psi_i}^+ + f_{\psi_{i+1}}^- = 0 \quad f_{F_i}^+ + f_{F_{i+1}}^- = 0 \quad f_{M_i}^+ + f_{M_{i+1}}^- = 0 \tag{B.10}$$

where,

$$f_{u_i}^\pm = \pm C^T C^{ab} F_i - \bar{f}_i^\pm \tag{B.11}$$

$$f_{\psi_i}^\pm = \pm C^T C^{ab} M_i - \bar{m}_i^\pm - \frac{\Delta L_i}{2} \left[(\tilde{e}_1 + \tilde{\gamma}_1) F_i \right] \tag{B.12}$$

$$f_{F_i}^\pm = \pm u_i - \frac{\Delta L_i}{2} \left[C^T C^{ab}(e_1 + \gamma_1) - C^{ab} e_1 \right] \tag{B.13}$$

$$f_{M_i}^\pm = \pm \theta_i - \frac{\Delta L_i}{2} \left[\Delta + \frac{\tilde{\theta}_i}{2} + \frac{\tilde{\theta}_i \tilde{\theta}_i^T}{4} \right] C^{ab} \kappa_i \tag{B.14}$$

$$\bar{f}_i^- = \int_0^1 (1 - \epsilon) f_a \Delta L_i d\epsilon \qquad \bar{f}_i^+ = \int_0^1 \epsilon f_a \Delta L_i d\epsilon \tag{B.15}$$

$$\bar{m}_i^- = \int_0^1 (1-\epsilon) m_a \Delta L_i d\epsilon \qquad \bar{m}_i^+ = \int_0^1 \epsilon m_a \Delta L_i d\epsilon \qquad \text{(B.16)}$$

The one-dimensional strains along the beam reference line are determined using the following equations:

$$\begin{bmatrix} \gamma \\ \kappa \end{bmatrix} = S \begin{bmatrix} F \\ M \end{bmatrix} \qquad \text{(B.17)}$$

References

Bohara, R.P., Linforth, S., Nguyen, T., Ghazlan, A., Ngo, T., 2021. Novel lightweight high-energy absorbing auxetic structures guided by topology optimisation. Int. J. Mech. Sci. 211, 106793. http://dx.doi.org/10.1016/j.ijmecsci.2021.106793.

Du, L., Luo, S., Xu, Y., 2022. Understanding nonlinear behaviors of auxetic foams using X-ray tomography and pore structure analysis. Mech. Mater. 165, 104196. http://dx.doi.org/10.1016/j.mechmat.2021.104196.

Dundar, M.A., Dhaliwal, G.S., Ayorinde, E., Al-Zubi, M., 2021. Tensile, compression, and flexural characteristics of acrylonitrile–butadiene–styrene at low strain rates: Experimental and numerical investigation. Polym. Polym. Compos. 29 (5), 331–342. http://dx.doi.org/10.1177/0967391120916619.

Dutta, S., Menon, H.G., Hariprasad, M., Krishnan, A., Shankar, B., 2021. Study of auxetic beams under bending: A finite element approach. Mater. Today: Proc. 46, 9782–9787. http://dx.doi.org/10.1016/j.matpr.2020.10.479, International Mechanical Engineering Congress 2019.

Einav, I., Houlsby, G., Nguyen, G., 2007. Coupled damage and plasticity models derived from energy and dissipation potentials. Int. J. Solids Struct. 44 (7), 2487–2508. http://dx.doi.org/10.1016/j.ijsolstr.2006.07.019.

Elipe, J.C.Á., Lantada, A.D., 2012. Comparative study of auxetic geometries by means of computer-aided design and engineering. Smart Mater. Struct. 21 (10), 105004. http://dx.doi.org/10.1088/0964-1726/21/10/105004.

Fu, M., Liu, F., Hu, L., 2018. A novel category of 3D chiral material with negative Poisson's ratio. Compos. Sci. Technol. 160, 111–118. http://dx.doi.org/10.1016/j.compscitech.2018.03.017.

Gao, Q., Wang, L., Zhou, Z., Ma, Z., Wang, C., Wang, Y., 2018. Theoretical, numerical and experimental analysis of three-dimensional double-V honeycomb. Mater. Des. 139, 380–391. http://dx.doi.org/10.1016/j.matdes.2017.11.024.

Gaspar, N., Ren, X., Smith, C.W., Grima, J.N., Evans, K.E., 2005. Novel honeycombs with auxetic behaviour. Acta Mater. 53, 2439–2445. http://dx.doi.org/10.1016/j.actamat.2005.02.006.

Gatt, R., Attard, D., Farrugia, P.-S., Azzopardi, K., Mizzi, L., Brincat, J.-P., Grima, J., 2013. A realistic generic model for anti-tetrachiral systems. Phys. Status Solidi (b) http://dx.doi.org/10.1002/pssb.201384246.

Grima, J., Gatt, R., Alderson, A., Evans, K., 2005. On the potential of connected stars as auxetic systems. Mol. Simul. 31, 925–935. http://dx.doi.org/10.1080/08927020500401139.

Hodges, D., 2006. Nonlinear Composite Beam Theory. AIAA, http://dx.doi.org/10.2514/4.866821.

Hu, L., Luo, Z., Zhang, Z., Lian, M., Huang, L., 2019. Mechanical property of re-entrant anti-trichiral honeycombs under large deformation. Composites B 163, 107–120. http://dx.doi.org/10.1016/j.compositesb.2018.11.010.

Jiang, Y., Rudra, B., Shim, J., Li, Y., 2019. Limiting strain for auxeticity under large compressive Deformation: Chiral vs. re-entrant cellular solids. Int. J. Solids Struct. 162, 87–95. http://dx.doi.org/10.1016/j.ijsolstr.2018.11.035.

Joseph, A., Mahesh, V., Harursampath, D., 2021. On the application of additive manufacturing methods for auxetic structures: a review. Adv. Manuf. 9 (3), 342–368. http://dx.doi.org/10.1007/s40436-021-00357-y.

Kachanov, L., 1999. Rupture time under creep conditions. Int. J. Fract. 97, 11—-18. http://dx.doi.org/10.1023/A:1018671022008.

Kolken, H.M.A., Zadpoor, A.A., 2017. Auxetic mechanical metamaterials. RSC Adv. 7, 5111–5129. http://dx.doi.org/10.1039/C6RA27333E.

Koudelka, P., Jiroušek, O., Fíla, T., Doktor, T., 2016. Compressive properties of auxetic structures produced with direct 3D printing. Mater. Tehnologije 50, 311–317. http://dx.doi.org/10.17222/mit.2014.204.

Levy, O., Krylov, S., Goldfarb, I., 2006. Design considerations for negative Poisson ratio structures under large deflection for MEMS applications. Smart Mater. Struct. 15 (5), 1459. http://dx.doi.org/10.1088/0964-1726/15/5/035.

Li, J., Jia, Y., Li, T., Zhu, Z., Zhou, H., Peng, X., Jiang, S., 2020. Tensile behavior of acrylonitrile butadiene styrene at different temperatures. Adv. Polym. Technol. 2020, http://dx.doi.org/10.1155/2020/8946591.

Li, C., Shen, H.-S., Wang, H., 2021. Full-scale finite element modeling and nonlinear bending analysis of sandwich plates with functionally graded auxetic 3D lattice core. J. Sandw. Struct. Mater. 23 (7), 3113–3138. http://dx.doi.org/10.1177/1099636220924657.

Liu, W., Li, H., Yang, Z., Zhang, J., Ge, X., 2020. In-plane elastic properties of a 2D chiral cellular structure with V-shaped wings. Eng. Struct. 210, 110384. http://dx.doi.org/10.1016/j.engstruct.2020.110384.

Madke, R.R., Chowdhury, R., 2020. Anti-impact behavior of auxetic sandwich structure with braided face sheets and 3D re-entrant cores. Compos. Struct. 236, 111838. http://dx.doi.org/10.1016/j.compstruct.2019.111838.

Meena, K., Singamneni, S., 2021. Novel hybrid auxetic structures for improved in-plane mechanical properties via additive manufacturing. Mech. Mater. 158, 103890. http://dx.doi.org/10.1016/j.mechmat.2021.103890.

Mousanezhad, D., Haghpanah, B., Ghosh, R., Hamouda, A.M., Nayeb-Hashemi, H., Vaziri, A., 2016. Elastic properties of chiral, anti-chiral, and hierarchical honeycombs: A simple energy-based approach. Theor. Appl. Mech. Lett. 6 (2), 81–96. http://dx.doi.org/10.1016/j.taml.2016.02.004.

Mukhopadhyay, T., Adhikari, S., 2016. Effective in-plane elastic properties of auxetic honeycombs with spatial irregularity. Mech. Mater. 95, 204–222. http://dx.doi.org/10.1016/j.mechmat.2016.01.009.

Mukhopadhyay, T., Adhikari, S., 2017. Effective in-plane elastic moduli of quasi-random spatially irregular hexagonal lattices. Internat. J. Engrg. Sci. 119, 142–179. http://dx.doi.org/10.1016/j.ijengsci.2017.06.004.

Najafi, M., Ahmadi, H., Liaghat, G., 2021. Experimental investigation on energy absorption of auxetic structures. Mater. Today: Proc. 34, 350–355. http://dx.doi.org/10.1016/j.matpr.2020.06.075, 12th International Conference on Composite Science and Technology.

Peng, X.-L., Bargmann, S., 2021. A novel hybrid-honeycomb structure: Enhanced stiffness, tunable auxeticity and negative thermal expansion. Int. J. Mech. Sci. 190, 106021. http://dx.doi.org/10.1016/j.ijmecsci.2020.106021.

Prajwal, P., Ghuku, S., Mukhopadhyay, T., 2022. Large-deformation mechanics of anti-curvature lattice materials for mode-dependent enhancement of non-linear shear modulus. Mech. Mater. 171, 104337. http://dx.doi.org/10.1016/j.mechmat.2022.104337.

Rad, M., Ahmad, Z., Alias, A., 2015. Computational approach in formulating mechanical characteristics of 3D star honeycomb auxetic structure. Adv. Mater. Sci. Eng. 2015, 1–11. http://dx.doi.org/10.1155/2015/650769.

Remennikov, A., Kalubadanage, D., Ngo, T., Mendis, P., Alici, G., Whittaker, A., 2019. Development and performance evaluation of large-scale auxetic protective systems for localised impulsive loads. Int. J. Prot. Struct. 10 (3), 390–417. http://dx.doi.org/10.1177/2041419619858087.

Sabari, S., Andrade, D., Leitão, C., Simões, F., Rodrigues, D., 2023. Influence of the strain hardening behaviour on the tensile and compressive response of aluminium auxetic structures. Compos. Struct. 305, 116472. http://dx.doi.org/10.1016/j.compstruct.2022.116472.

Scarpa, F., Panayiotou, P., Tomlinson, G., 2000. Numerical and experimental uniaxial loading on in-plane auxetic honeycombs. J. Strain Anal. Eng. Des. 35 (5), 383–388. http://dx.doi.org/10.1243/0309324001514152.

Seetoh, I.P., Liu, X., Markandan, K., Zhen, L., Lai, C.Q., 2021. Strength and energy absorption characteristics of Ti6Al4V auxetic 3D anti-tetrachiral metamaterials. Mech. Mater. 156, 103811. http://dx.doi.org/10.1016/j.mechmat.2021.103811.

Smith, C., Grima, J., Evans, K., 2000. A novel mechanism for generating auxetic behaviour in reticulated foams: missing rib foam model. Acta Mater. 48 (17), 4349–4356. http://dx.doi.org/10.1016/S1359-6454(00)00269-X.

Srivastava, C., Bhola, L., Mahesh, V., Guruprasad, P.J., Petrinic, N., Scarpa, F., Harursampath, D., Ponnusami, S.A., 2023a. Exploiting nonlinearities through geometric engineering to enhance the auxetic behaviour in re-entrant honeycomb metamaterials. Sci. Rep. 13, http://dx.doi.org/10.1038/s41598-023-47525-7.

Srivastava, C., Mahesh, V., Pitchai, P., Guruprasad, P.J., Petrinic, N., Scarpa, F., Harursampath, D., Ponnusami, S.A., 2023b. Effective mechanical properties of auxetic materials: Numerical predictions using variational asymptotic method based homogenization. J. Appl. Mech. 90 (11), 111001. http://dx.doi.org/10.1115/1.4062845.

Tabacu, S., Negrea, R.F., Negrea, D., 2020. Experimental, numerical and analytical investigation of 2D tetra-anti-chiral structure under compressive loads. Thin-Walled Struct. 155, 106929. http://dx.doi.org/10.1016/j.tws.2020.106929.

Tang, C., Li, L., Wang, L., Herencia, V.Z., Ren, J., 2020. Numerical and experimental studies on the deformation of missing-rib and mixed structures under compression. Phys. Status Solidi (b) 257, http://dx.doi.org/10.1002/pssb.202000150.

Theocaris, P., Stavroulakis, G., Panagiotopoulos, P., 1997. Negative Poisson's ratios in composites with star-shaped inclusions: A numerical homogenization approach. Arch. Appl. Mech. 67, 274–286. http://dx.doi.org/10.1007/s004190050117.

Voyiadjis, G.Z., Kattan, P.I., 2022. The True Nature of the Decomposition of the Damage Variable. Springer International Publishing, Cham, pp. 3–22.

Wan, H., Ohtaki, H., Kotosaka, S., Hu, G., 2004. A study of negative Poisson's ratios in auxetic honeycombs based on a large deflection model. Eur. J. Mech. A Solids 23 (1), 95–106. http://dx.doi.org/10.1016/j.euromechsol.2003.10.006.

Wang, Y., 2022. Auxetic composite laminates with through-thickness negative Poisson ratio for mitigating low velocity impact damage: A numerical study. Materials 15 (19), http://dx.doi.org/10.3390/ma15196963.

Wang, T., Wang, L., Ma, Z., Hulbert, G.M., 2018. Elastic analysis of auxetic cellular structure consisting of re-entrant hexagonal cells using a strain-based expansion homogenization method. Mater. Des. 160, 284–293. http://dx.doi.org/10.1016/j.matdes.2018.09.013.

Wei, L., Zhao, X., Yu, Q., Zhu, G., 2020. A novel star auxetic honeycomb with enhanced in-plane crushing strength. Thin-Walled Struct. 149, 106623. http://dx.doi.org/10.1016/j.tws.2020.106623.

Xue, J., Kirane, K., 2021. Effect of the shape of the softening damage law on the predicted tensile fracturing and energy dissipation in textile composites. Int. J. Damage Mech. 30, http://dx.doi.org/10.1177/1056789520986849.

Yang, L., Harrysson, O., West, H., Cormier, D., 2015. Mechanical properties of 3D re-entrant honeycomb auxetic structures realized via additive manufacturing. Int. J. Solids Struct. 69–70, 475–490. http://dx.doi.org/10.1016/j.ijsolstr.2015.05.005.

Yu, W., Blair, M., 2012. GEBT: A general-purpose nonlinear analysis tool for composite beams. Compos. Struct. 94 (9), 2677–2689. http://dx.doi.org/10.1016/j.compstruct.2012.04.007.

Yu, W., Hodges, D., Hong, X., Volovoi, V., 2002. Validation of the variational asymptotic beam sectional analysis. Aiaa J. - AIAA J 40, 2105–2112. http://dx.doi.org/10.2514/2.1545.

Zhang, J., Lu, G., You, Z., 2020. Large deformation and energy absorption of additively manufactured auxetic materials and structures: A review. Composites B 201, 108340. http://dx.doi.org/10.1016/j.compositesb.2020.108340.